Prime editing via PE2max rescues galactosylceramidase function and neurobehavioral deterioration in Krabbe disease

Kim, Min kyoung

Department of Biomedical Engineering

Graduate School

Yonsei University

Prime editing via PE2max rescues galactosylceramidase function and neurobehavioral deterioration in Krabbe disease

Advisor Cho, Sung-Rae

A Master's Thesis Submitted
to the Department of Biomedical Engineering
and the Committee on Graduate School
of Yonsei University in Partial Fulfillment of the
Requirements for the Degree of
Master of Biomedical Engineering

Kim, Min kyoung

July 2025

Prime editing via PE2max rescues galactosylceramidase function and neurobehavioral deterioration in Krabbe disease

This Certifies that the Master's Thesis of
Kim, Min kyoung is Approved

Committee Chair _____

Cho, Sung-Rae

Committee Member _____

Kim, Hyongbum

Committee Member _____

Yoo, Heechan

Department of Biomedical Engineering
Graduate School
Yonsei University
July 2025

ACKNOWLEDGEMENTS

The master's program has been a valuable opportunity for self-reflection and deeper learning.

I am sincerely grateful to my labmates who shared long nights, who offered generous advice and insights, and to younger colleagues for their steady support.

I would also like to express my deepest respect and gratitude to my advisor, Professor Sung-Rae Cho, for guiding me to stay grounded as a researcher, and to Professor Hee-Chan Yoo, for his generous support that allowed me to focus fully on my work.

From designing experiments to analyzing data and writing this thesis, none of it could have been done alone. I extend my heartfelt thanks to everyone who helped me in their own way throughout this journey.

And above all, I owe my deepest love and gratitude to my family, who have stood by me in every moment with unwavering support and endless love.

"You must never think of the whole road at once. Just think of the next step, the next breath, the next sweep of the broom. That's how it works."

— Beppo the street sweeper, Momo by Michael Ende

I try to live each day with sincerity, letting life unfold as it will—reminding myself that what matters most is the heart to simply keep going, even when things break down.

I will continue to face challenges, solve problems, and grow into a scientist who focuses on one step at a time.

Thank you.

감사의 글

석사 과정은 제 모습을 새롭게 발견하고, 많은 것을 배운 시간이었습니다.
연구실에서 함께 밤을 지새우며 서로에게 힘이 되어준 동기들, 조언과 경험을 아낌없이 나눠주신 선배들, 한결같은 응원을 보내준 후배들에게 깊은 감사의 마음을 전합니다.
연구자로서의 중심을 잃지 않도록 이끌어주신 조성래 지도교수님과, 연구에 온전히 몰두할 수 있도록 아낌없는 지원을 보내주신 유희찬 교수님께 깊은 존경과 감사를 드립니다.
실험 설계부터 데이터 분석, 논문 작성에 이르기까지의 모든 과정은 결코 혼자의 힘만으로 완성할 수 없었습니다. 각자의 방식으로 아낌없이 도움을 주신 모든 분들께 이 자리를 빌려 진심으로 감사의 마음을 전합니다.
그리고 무엇보다, 모든 순간을 함께하며 흔들림 없는 지지와 무한한 사랑을 보내준 가족들에게 깊은 감사와 사랑을 전합니다.

“한꺼번에 도로 전체를 생각해서는 안 돼. 다음에 딛게 될 한 걸음, 쉬게 될 한 호흡, 한 번의 비질에 집중하다 보면, 어느새 길을 다 쓸었다는 걸 알게 돼. 어떻게 그렇게 했는지도 모르겠고, 숨이 차지도 않아.”
— 『모모』 중 베포 거리 청소부의 말

하루하루는 성실하게, 인생 전체는 되는대로, 중요한 건 꺾여도 다시 일어나는 마음이라는 것을 잊지 않으려 합니다.
앞으로도 갈등을 마주하고, 문제를 해결하며, 한 걸음에 집중하는 과학자가 되겠습니다.

감사합니다.

TABLE OF CONTENTS

LIST OF FIGURES

LIST OF TABLES

ABSTRACT

Prime editing via PE2max rescues galactosylceramidase function and neurobehavioral deterioration in a Krabbe disease

Krabbe disease (KD) is a life-threatening lysosomal storage disorder caused by mutations in the galactosylceramidase (GALC) gene, leading to psychosine accumulation, demyelination, and neurodegeneration in the central nervous system (CNS) and peripheral nervous system (PNS). Prime editing (PE) is a genome-editing method that allows for accurate base substitutions and small insertions or deletions without introducing double-strand DNA breaks. This study proposes a therapeutic strategy for KD using PE with the PE2max system to correct a point mutation and restore *Galc* function in Twitcher mice. Precise A-to-G correction at the *Galc* locus restored *Galc* expression and enzymatic activity, markedly enhancing molecular, histological, and behavioral measures. At postnatal day 1, PE2max was delivered via dual-adeno-associated virus (AAV) strategy: AAV-PHP.eB for CNS targeting and AAV-MaCPNS1 for PNS delivery. Deep genomic DNA and cDNA sequencing confirmed high editing fidelity with minimal off-target effects and background-level insertions/deletions (indels). CNS regions—including the frontal cortex, brainstem, and spinal cord—exhibited higher editing efficiency than other dissected regions, correlating with increased *Galc* mRNA expression and enzymatic activity. These effects were further supported by increased myelin basic protein expression, enhanced myelin integrity, and reduced globoid cell infiltration. Consistently, magnetic resonance imaging showed preserved white matter, and transmission electron microscopy revealed compact myelin and intact axons, indicating recovery at the macro- and ultrastructural levels. Although the extent of sciatic nerve editing was modest, the safety profile was excellent, with no observable toxicity in either wild-type or mutant mice.

Our findings confirm that PE2max-mediated PE is a precise and safe *in vivo* genome-editing strategy that corrects disease-causing mutations without introducing double-strand breaks, supporting its therapeutic potential for monogenic neurodegenerative disorders.

Keywords: Krabbe disease, neurodegenerative disease, gene editing, prime editing, galactosylceramidase, myelin, demyelination

I. INTRODUCTION

Krabbe disease (KD), also known as globoid cell leukodystrophy (GCL), is a rare and life-threatening lysosomal storage disorder caused by galactosylceramidase (GALC) deficiency.[1,2]. GALC is crucial for the degradation of galactolipids, such as galactosylceramide (GalCer) and psychosine, which are essential for preserving myelin integrity[3-5]. The loss of GALC function results in the toxic accumulation of psychosine, a metabolite that mainly targets oligodendrocytes and Schwann cells[4,6-8]. Psychosine aggregates are particularly prominent in the white matter of the brain and the sciatic nerves (SNs), where they disrupt essential cellular processes and trigger glial cell apoptosis[4,9,10]. This cellular damage results in widespread demyelination across the central nervous system (CNS) and peripheral nervous system (PNS) and contributes to the hallmark pathological features of KD, including oligodendrocyte loss, reactive astrocytosis, and infiltration of multinucleated phagocytes known as globoid cells[4,7,8,11]. KD is clinically characterized by progressive motor and cognitive decline, muscle stiffness, spasticity, and developmental regression, with early infantile-onset cases being the most common and severe[12-14]. Despite advances in therapeutic strategies, such as hematopoietic stem cell transplantation (HSCT), current treatments can only slow down disease progression, highlighting the need for novel therapies to address neurodegeneration in KD[15-17]. Prime editing (PE) is a genome-editing technique that allows for precise genetic modifications without introducing double-strand breaks (DSBs)[18,19]. Unlike conventional CRISPR-based methods that rely on error-prone DNA repair pathways, PE utilizes a Cas9 nickase (H840A) fused with a reverse transcriptase and a PE guide RNA (pegRNA) to direct the desired genetic modification[20,21] . This system facilitates targeted base substitutions as well as small insertions and deletions while minimizing the risk of unintended genomic alterations, such as large deletions or chromosomal rearrangements[18,22]. Owing to its precision and versatility, PE has been successfully applied in various biological systems, including mammalian cells, plants, and model organisms, making it a promising strategy for therapeutic applications and functional

genomics[19,20,23]. As a monogenic loss-of-function disorder, KD is an ideal candidate for gene therapy. Adeno-associated viruses (AAVs) are a preferred vehicle for gene therapy owing to their broad tissue tropism, low immunogenicity, and capacity to sustain long-term gene expression[19,24 25-27]. However, AAV vectors are limited by a small packaging capacity of approximately 4.7 kb, which limits their ability to deliver larger genome-editing agents such as PE, which has a size of 6.3 kb[28-30]. In addition, although AAVs can transduce various tissues, systemic injections alone often fail to achieve efficient transduction of the CNS, thereby necessitating invasive methods, such as intrathecal or intraventricular injections[31]. Although these strategies have proven effective, they remain insufficient when therapeutic gene delivery is required to target the entire nervous system or widely distributed cellular populations[28,32]. To overcome these drawbacks, novel AAV capsids, such as AAV-PHP.eB and AAV-MaCPNS1, have been developed to enhance transduction efficiency in the CNS and PNS[28,33]. Moreover, the use of a split intein-fused system enables packaging of large genome-editing agents, such as PE, into two separate AAV vectors that can be co-delivered, effectively overcoming the size limitations of traditional AAV vectors.

We herein report the successful use of the PE2max PE system to directly correct a PTC-causing point mutation in the *Galc* gene of twitcher (Twi) mice (*Galc*$^{twi/twi}$).

Although base editors have been used in a range of genetic disorders, their potential for use in currently untreatable neurodegenerative diseases, such as KD, remains to be investigated. In addition, we demonstrated the *in vivo* safety of PE treatment via a dual-AAV9 delivery system in Twi mice, providing strong support for the clinical potential of PE in treating KD.

2. MATERIALS AND METHODS

2.1. Vector design and optimization

PE2max was split into two AAV vectors owing to its large size, with each construct driven by a CMV (cytomegalovirus) promoter. Using the Npu-intein system, the N- and C-terminal halves of PE2max were packaged into separate vectors, with the C-terminal vector also carrying a U6 promoter-driven epegRNA cassette. At P1, a total dose of 4×10^9 vg (2×10^9 vg per vector) was administered via facial vein injection. All viral vectors were stored at −80°C in deep freezer. These dual AAV constructs were kindly provided by Prof. Heechan Yoo (Chung-Ang University).

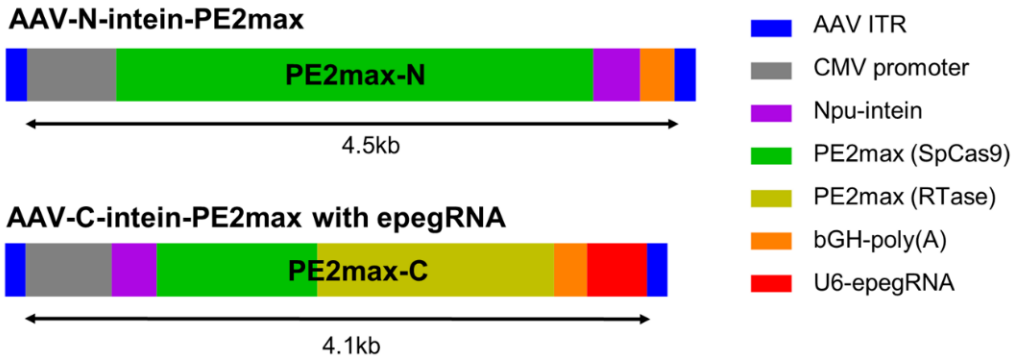

Figure 1. Schematic diagram of split PE2max AAV constructs for prime editor.
The architectures of the two types of vectors used in this study are presented. The top diagram illustrates PE2max-NT, the N-terminal half with SpCas9, driven by a CMV promoter and fused to Npu-intein. The bottom diagram shows PE2max-CT, the C-terminal half with reverse transcriptase, also fused to Npu-intein, plus a U6-driven epegRNA cassette and a bGH poly(A) signal.

2.2. Mutant *Galc* human embryonic kidney 293 (HEK293T) cells

HEK293T cells were transduced with lentivirus carrying a mutant *Galc* sequence and selected using ampicillin to enrich fully infected cells. The mutant sequence matched the point mutation and flanking regions observed in the Twi mouse model. The mutation introduces a premature stop codon, mimicking the loss-of-function phenotype observed in KD.

2.3. Animals and housing conditions

The mutant strain (B6.CE-*Galc*^{twi}/J, JAX comprehensive protocol #000845), which was supplied by Jackson Laboratory (USA), was maintained under specific pathogen-free conditions. The *Galc*^{twi} mutation involves G-to-A transition at codon 355 of the *Galc* gene, creating a stop codon. Symptoms occur at approximately day 21, with death typically occurring by day 40. To create wild-type (WT) and homozygous Twi mice, heterozygous mice were bred. All heterozygous Twi mice were housed in standard cages (27 × 22.5 × 14 cm^3) for the same duration. They were provided with food and water *ad libitum* and kept under a 12-h light/dark cycle in accordance with animal protection regulations. This study was approved by the Institutional Animal Care and Use Committee (IACUC) of Yonsei University Health System (permit number: 2023-0219, 2024-0196).

2.4. Neonatal Intravenous injection on postnatal day 1

At postnatal day 1 (P1), intravenous (IV) viral delivery via the facial vein was performed. The AAV-PHP.eB and AAV-MaCPNS1 vectors were mixed at a 1:1 ratio and administered at a total dose of 2 × 10^{11} viral genomes (vg) per pup. For each injection, 30 μL of the viral mixture, supplemented with Evans blue dye for visualization, was delivered using a 31-gauge insulin syringe. The Twi and WT neonatal mice received IV injections for the evaluation of not only therapeutic efficacy but also the safety of the viral constructs. Subsequently, the pups were immediately returned to their home cage with the dam.

2.5. Experimental protocol

At P1, IV injection was performed, and genotyping was conducted before P21 (Figure 3). Behavioral tests and body weight measurements were performed at weeks 3, 4, and 5 to evaluate neurological function improvement. The mice were sacrificed on P38 (Figure 2).

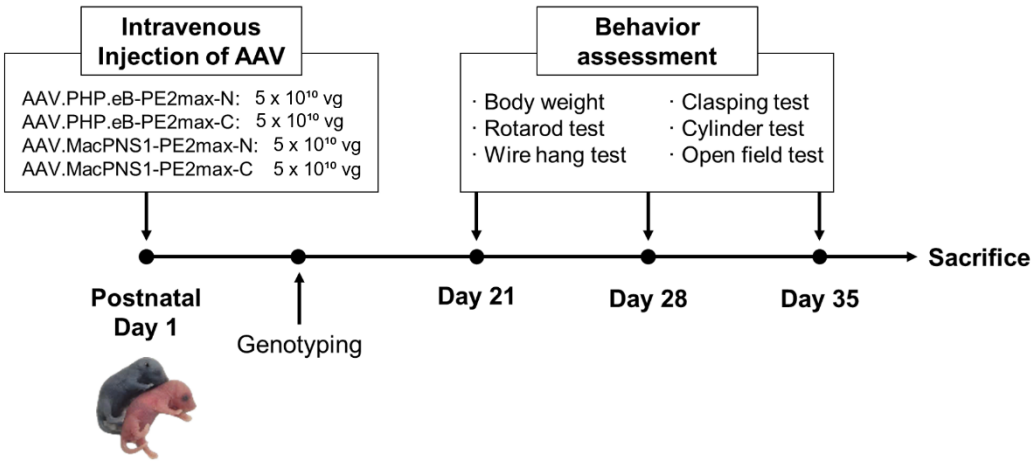

Figure 2. Experimental scheme detailed timeline.

This figure presents the experimental schedule for AAV injection and subsequent behavioral evaluation.

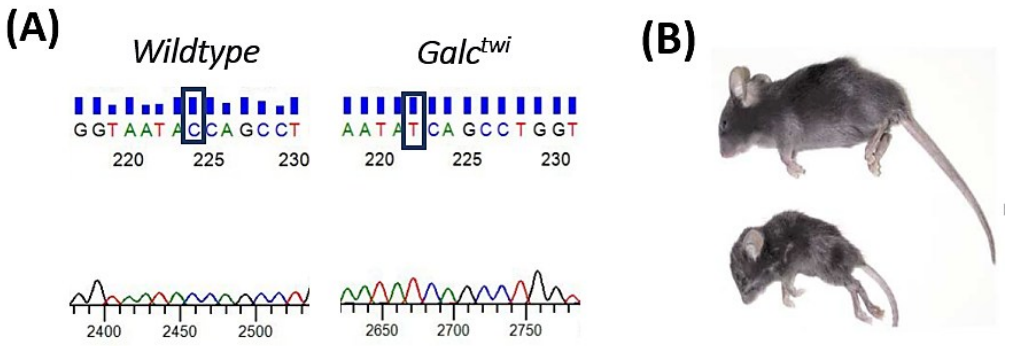

Figure 3. Genotype for identification.

(A) The PCR products were subjected to Sanger sequencing for the genotype determination. Mice homozygous for the cytidine allele (CCAGCCT) were identified as WT, whereas those homozygous for the thymine allele (TCAGCCT) were identified as twitcher mutants. (B) The phenotypes of WT and twitcher mice were compared. Adapted from Kobayashi et al. [34].

2.6. Behavioral assessment

(A) Rotarod test: To evaluate motor coordination and locomotor performance, the mice were placed on a rotarod treadmill (Ugo Basile, Gemonio, Italy). The latency to fall—defined as the duration the mouse stayed on the rotating rod—was measured. Rotarod testing was conducted once a week for 3 consecutive weeks at a constant speed of 4 rpm. Latency was recorded during the third trial of each session, with a maximum allowable duration of 300 s.

(B) Cylinder test: This test was employed to evaluate spontaneous locomotor activity, motor function, and forelimb use asymmetry in rodents. Mice were placed individually in a transparent cylinder, where their natural behavior of rearing on their hind limbs and exploring the environment with their forelimbs was observed. During a 5-min observation period, the number of rearings was recorded as an exploratory behavioral measure.

(C) Clasping test: This test was employed to evaluate motor asymmetry and exploratory behavior in mouse models of neurodegenerative disease. In a single trial, mice aged 3–5 weeks were suspended by their tail for 10 s. The scoring was based on the hindlimb clasping duration: 0 points for no clasping, 1 point for 1–5 s, 2 points for 5–10 s, and 3 points for 10 s.

(D) Wire hanging test: This test was used to evaluate neuromuscular strength. Mice were suspended by their forelimbs from a wire positioned 30 cm above the bedding. The maximum latency to fall was recorded across three trials per session, with a 10-min rest period between trials. The maximum allowable duration was 300 s.

(E) Open field test: The apparatus consisted of a square chamber (50 × 50 × 38 cm) made of white, high-density, nonporous plastic. Mice were allowed to freely explore within the chamber for 25 min. Movement was tracked and analyzed using SMART Video Tracking (PanLab/Harvard Apparatus).

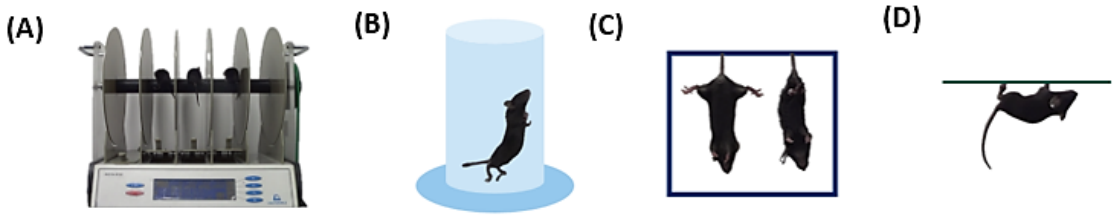

Figure 4. Represent image of behavioral assessment.

(A) Image of the rotarod test, (B) cylinder test, (C) clasping test, and (D) wire hanging test.

2.7. Sacrificed

At P38, mice were anesthetized using ketamine (100 mg/kg) and Rompun (10 mg/kg) and then placed in a dark, comfortable cage for over 5 min to ensure that the anesthesia took effect. After cardiac perfusion with PBS, the brain and abdominal organs (heart, lung, liver, spleen, kidney, spinal cord (SC), and SN) were collected. Samples intended for molecular studies were stored in a deep freezer at −80°C, whereas those for histological studies were fixed in 4% paraformaldehyde (PFA) and subsequently preserved in a 30% sucrose solution at 4°C.

2.8. Genomic DNA (gDNA) extraction

Using KAPA lysis buffer, genomic DNA was extracted from mouse ear clips. The genetic status of each mouse was determined via polymerase chain reaction (PCR)-based genotyping, in accordance with the protocol provided by The Jackson Laboratory.

2.9. RNA isolation

RNA extraction was performed from *in vivo* samples using TRIzol reagent (Invitrogen Life Technologies, Carlsbad, CA, USA). RNA was precipitated with isopropanol, pelleted, and then washed with 75% ethanol. The isolated RNA was air-dried at room temperature for 30 min to allow evaporation of any residual washing solution. Subsequently, pellets were resuspended in 20 μL of DEPC-dH_2O. RNA was quantified at 260 nm using a spectrophotometer (Thermo Fisher Scientific; NanoDrop 2000C), and its purity was determined by measuring the A260/A280 ratio.

2.10. cDNA quantitative real-time polymerase chain reaction (qRT-PCR)

To generate complementary DNA (cDNA), reverse transcription was performed using ReverTra Ace-α- (TOYOBO, FSK-101) according to the manufacturer's protocols.

qRT-PCR was conducted in triplicate using the StepOnePlus Real-Time PCR system (Applied Biosystems, Foster City, CA, USA) and 2xqPCRBIO SyGreen Mix (PB20.12-05, PCR Biosystems, London, UK), with the following thermocycler conditions: amplifications start with a template preincubation step at 95°C for 300 s, followed by 45 cycles at 95°C for 10 s, 60°C for 10 s, and 72°C for 10 s. All samples were analyzed in triplicate, and the relative expression of the target RNAs was calculated using the $\Delta\Delta C_t$ of the gene of interest compared with the housekeeper gene. Table 2 lists the primer sequences used in this study.

Table 1. Primer sequences for qRT-PCR

Name	Forward primer (5'→3')	Reverse primer (5'→3')
PE2max-NT	CGT GGA GAA GAG GAT CGA GTG	CTC CTG CTC TCC CCT ATC GT
PE2max-CT	ACG GAA ATA CCT GGG AAA GCA	TAA AGC CAT TCT TCA GGG CGA
Galc	AGG TCT CCA GCG AGT GAG AAT CAT AG	TGT GTG AGC TGA TAC CCA GAT AGG AG
Gapdh	GTG GAG CCA AAA GGG TCA TCA	CCC TTC CAC AAT GCC AAA GTT

Notes: *Gapdh*, glyceraldehyde-3-phosphate dehydrogenase; *Galc*, galactosylceramidase

2.11. High-throughput sequencing (HTS)

The target sites of the *Galc* gene were amplified from either genomic DNA or cDNA using SUN-PCR blend (Sun Genetics). Then, PCR products were purified using Expin PCR SV mini (GeneAll) and sequenced using a MiniSeq Sequencing System (Illumina). The results were analyzed using BE-Analyzer (http://www.rgenome.net/be-analyzer/).

2.12. GALC enzyme activity

GALC enzyme activity was evaluated using a β-galactosidase competitive inhibition assay. Brain tissue was homogenized on ice in distilled water using a pellet pestle and then sonicated twice for 20 s while kept on ice. A reaction mixture with 5 μg of brain homogenate and GALC substrate (6HMU-β-d-galactoside, Moscerdam Substrates, Rotterdam, Netherlands) was incubated at 37° C for 17 h. Fluorescence was measured (λex = 404 nm, λem = 460 nm) using an Envision high-throughput sequencing multimode plate reader (PerkinElmer, Hamburg, Germany).

2.13. Psychosine levels

To minimize sphingolipid adsorption, mouse brain hemispheres were weighed and homogenized in 1.2 mL of 1× PBS using a stainless-steel homogenizer. The Bradford assay was employed to determine protein concentrations. The homogenates were spiked with 4.2 μL of internal standard (N,N-dimethyl-D-galactosyl-β1-1'-D-sphingosine, 1,000 ppb), followed by sequential addition of 2-mL methanol and 1-mL chloroform. After a 60-s sonication at room temperature (amplitude: 20%, pulse: 0), the samples were incubated overnight at 48 °C. The next day, the samples were cooled at room temperature for at least 1 h and then mixed with 452 μL of 1 M KOH. After another 60-s sonication, the tubes were incubated at 37 °C for 2–3 h and cooled again for a minimum of 15 min. Subsequently, 24.4 μL of glacial acetic acid was added, followed by vortexing for 20 s. The samples were then aliquoted into 1.5 mL of low-adhesion tubes (300 μL per tube) and dried overnight using a speed vacuum concentrator at 25°C. The dried residues were reconstituted in

400 μL of chloroform/methanol (1:2, v/v) via vortexing and pipetting. After centrifugation at 1,800 × g for 15 min at 4 °C, the supernatants were collected and stored at −20 °C until analysis via high-resolution LC-MS (Thermo Fisher Exploris 240).

2.14. Immunofluorescence (IF)

Mouse brain and SC samples were postfixed overnight in 4% PFA, dehydrated in 30% sucrose at 4°C, embedded in OCT (Leica), rapidly frozen in isopentane cooled with dry ice, and sectioned into 16-μm slices using a cryostat (Leica Microsystems, Austria). For staining, the primary antibodies used were GALC (1:400; ABclonal) and myelin basic protein (MBP, 1:400; Abcam).

After washing with SD, the sections were incubated with fluorophore-conjugated secondary antibodies, followed by Alexa Fluor® 488 goat anti-rat secondary antibodies (1:400; Invitrogen) and Alexa Fluor® 594 goat anti-rabbit secondary antibodies (1:400; Invitrogen). Slides were mounted with Vectashield® mounting medium containing DAPI (4′,6-diamidino-2-phenylindole; Vector, Burlingame, CA, USA) and analyzed using an M2 microscope (Zeiss, Göttingen, Germany).

2.15. Luxol fast blue/Periodic acid-Schiff staining

Luxol fast blue (LFB) stains myelin blue, whereas Periodic Acid-Schiff (PAS) stains demyelinated axons pink. Tissue samples, including the brain and SC, were fixed in 4% PFA at 4°C and paraffin-embedded. Coronal sections of the corpus callosum (CC) region (4-μm thick) were prepared from the paraffin-embedded tissue samples. Deparaffinized sections were incubated overnight in 0.1% LFB solution at 70°C. Subsequently, the sections were washed with tap water and differentiated by dipping in 0.05% lithium carbonate solution and 70% ethanol until the gray matter appeared transparent. After dehydration, all sections were cleared in xylene and mounted using a mounting medium. The mean gray value of the stained regions was subsequently analyzed using ImageJ software.

2.16. Hematoxylin and eosin staining (H&E)

Nuclear (purple) and cytoplasmic (pink) regions were distinguished *in vivo*, and the staining patterns showed cell distribution and histopathological structure. This study investigated potential abnormalities, such as dysplasia.

2.17. Transmission electron microscopy (TEM)

The CC and SN were subjected to electron microscopic analysis. Mouse brains were harvested at P38 and immediately fixed in 0.1 M phosphate buffer, followed by fixation for over 12 h in 4% PFA containing 2% glutaraldehyde (MERCK, Darmstadt, Germany). Samples were postfixed in 1% osmium tetroxide dissolved in 0.1 M phosphate buffer for 2 h, dehydrated in ethanol, and infiltrated with propylene oxide. Embedding was performed using a Poly/Bed 812 kit (Polysciences, Warrington, PA, USA). For counterstaining, 70-nm ultra-thin sections were stained with 6% uranyl acetate (EMS, 22,400) for 20 min and lead citrate (Fisher) for 10 min. Sections were prepared using a LEICA EM UC-7 ultramicrotome (Leica Microsystems) and placed on copper and nickel grids. A JEM-1011 transmission electron microscope (JEOL, Japan) was used for the observations, and the numbers of myelin turns and axons were quantified from the images.

2.18. Diffusion tensor imaging metric acquisition and comparison

Magnetic resonance imaging (MRI) was performed at P38 on mice anesthetized with 1%–2% isoflurane. A 9.4 T Bruker BioSpec system (Ettlingen, Germany) equipped with a 40-mm transceiver coil and Paravision 5.1 software was used. Anatomical images were acquired using the RARE sequence. Diffusion imaging was performed using a diffusion tensor imaging (DTI)-EPI protocol and analyzed using DSI Studio (http://dsi-studio.labsolver.org). Comparisons were then performed between each group using four DTI parameters: FA, AD, RD, and MD. The imaging parameters used were as follows: slice thickness, 0.32 mm; number of slices, 20; matrix size, 128 × 128; matrix resolution, 0.156 × 0.156 mm; 4/10 ms; 30 directions with b = 670 s/mm^2; and TE/TR = 23.5/5000 ms.

2.19. Statistical analysis

Data are presented as mean ± standard error of the mean (SEM). Statistical significance was primarily assessed using one-way analysis of variance (ANOVA), followed by Bonferroni post hoc comparisons. For behavioral tests and longitudinal body weight measurements, two-way repeated-measures ANOVA was used to evaluate the interaction effect between time and treatment group. For lifespan and survival analyses, the estimated mean lifespan was analyzed via one-way ANOVA with Bonferroni correction. Cumulative survival curves were generated using the Kaplan–Meier method and analyzed with the log-rank (Mantel–Cox) test. Interval survival analysis between P36 and P49 was also performed using the log-rank test. Additionally, group-wise survival proportions were compared using chi-squared tests and visualized in gradient blue according to survival percentage and significance. Statistical significance is denoted as $*P < 0.05$, $**P < 0.01$, and $***P < 0.001$. All statistical analyses were conducted using SPSS software version 28.0 (IBM Corporation, Armonk, NY, USA), and graphs were plotted using GraphPad Prism version 9.

3. RESULTS

3.1. Optimization and selection of pegRNA for the KD mutation, subsequent *in vitro* confirmation.

A Twitcher (Twi) mouse serves as a genetically accurate model of KD, recapitulating the biochemical, histopathological, and clinical manifestations observed in humans. This model carries a nonsense mutation (W355X, G1065A) in the murine *Galc* gene, resulting in a premature termination codon that activates nonsense-mediated mRNA decay, ultimately leading to complete loss of GALC enzymatic activity.

To correct the G1065A mutation using PE, epegRNAs were used, which integrate structured RNA motifs at the 3′ terminus of pegRNA to enhance stability, prevent degradation, and increase editing efficiency. To optimize the epegRNA design, DeepPrime, a computational tool that predicts highly efficient PE constructs, was used. To evaluate the PE efficiency of the top six epegRNA candidates predicted by DeepPrime, a HEK293T cell line carrying the mutant *Galc* gene from the Twi mouse was engineered via lentiviral transduction, thereby mimicking pathogenic mutation (Figure 5). These cells were transiently transfected with the PE2max plasmid together with individual epegRNA plasmids, and PE efficiency was subsequently assessed. Based on our results, an epegRNA containing a 12-nucleotide primer binding site (PBS) and a 15-nucleotide reverse transcription template showed the highest PE efficiency at 8% (Figure 6). Moreover, Cas-OFFinder analysis revealed that off-target events were negligible with one to three mismatches and only became detectable at four mismatches, suggesting that the selected pegRNA has high specificity and minimal off-target potential (Table 2).

The split-intein PE2max system achieved PE efficiency (~8%) comparable to that of the single-vector system, highlighting its suitability for *in vivo* applications.

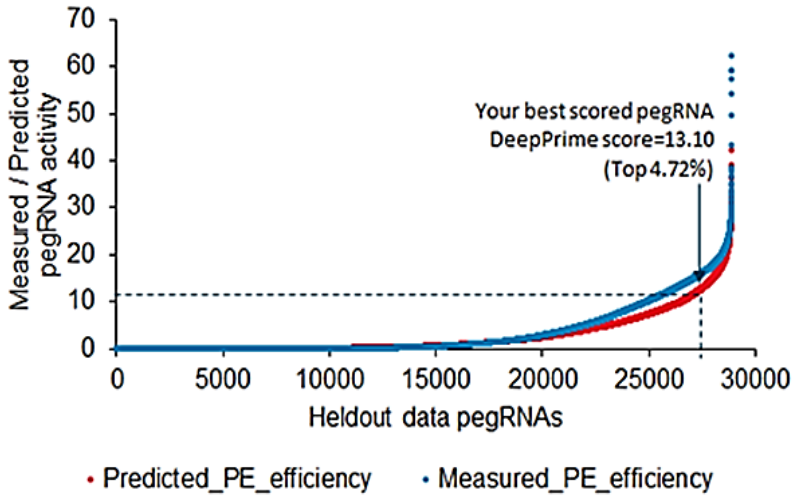

Figure 5. Evaluation of the predicted editing efficiency of pegRNA.

Optimal pegRNA sequences were predicted using DeepPrime (DeepPrime, https://deepcrispr.info/DeepPrime/). Scatter plot displaying DeepPrime-predicted prime editing efficiencies (red dots) alongside experimentally measured editing efficiencies (blue dots) across a held-out dataset of ~30,000 pegRNAs.

Table 2. Off-target number of pegRNA predicted by Cas-OFFinder.

Target Sequence	Bulge Type	Bulge Size	Mismatch	Number of Found Targets
GCAACCCAGTTTACTCAACCNGG	X	0	1	1
GCAACCCAGTTTACTCAACCNGG	X	0	3	3
GCAACCCAGTTTACTCAACCNGG	X	0	4	50

Note: The optimal pegRNA was selected based on the lowest off-target number. The pegRNA spacer sequence "GCAACCCAGTTTACTCAACC" was evaluated using Cas-OFFinder (http://www.rgenome.net/cas-offinder/).

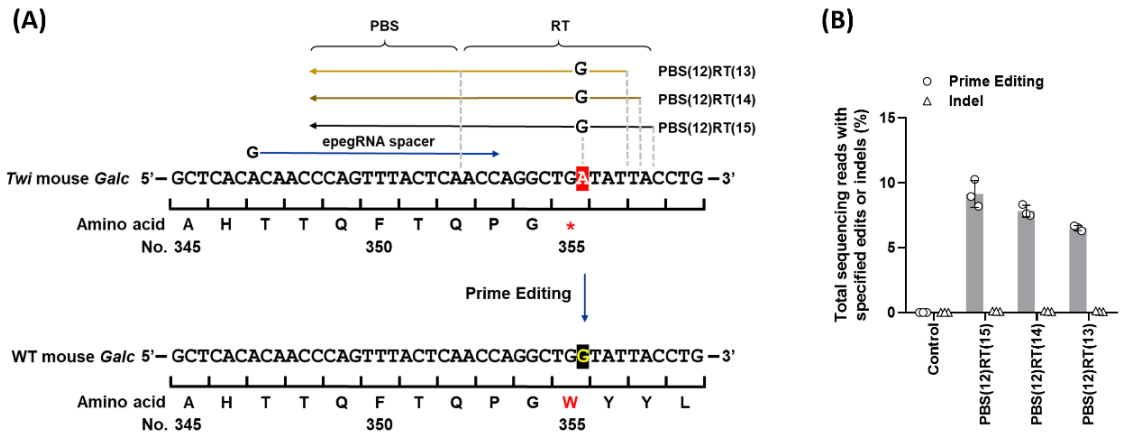

Figure 6. Quantification of editing and indel rates after prime editing with three pegRNA variants.

(A) Overview of the *Galc* sequence variation between Krabbe and wild-type mice and design of three pegRNAs targeting the mutation with a 12-nt PBS and 13–15-nt reverse transcription template. (B) Prime editing efficiency was measured in HEK293T cells carrying the mutant *Galc* allele, showing variable correction levels across pegRNA candidates.

3.2. Intravenous administration of AAV vectors led to systematic and organ-specific expression in the CNS and peripheral tissues

KD leads to CNS demyelination and progressive PNS degeneration, requiring systemic gene delivery to both systems. To achieve this, AAV-PHP.eB, which exhibits high CNS tropism, was employed alongside AAV-MaCPNS1, an engineered AAV capsid with preferential PNS transduction. AAV transduction efficiency is primarily determined by the expression of specific cell surface proteins that interact with the viral capsid. Notably, AAV-PHP.eB transduction is highly dependent on the presence of Ly6a, a gene expressed in the blood–brain barrier (BBB). However, studies investigating the transduction efficiency of AAV-PHP.eB and AAV-MaCPNS1 in neonatal mice remain scarce. To evaluate their capacity for tissue transduction at an early developmental stage, an AAV-mediated PE system was designed incorporating the split-intein PE2max system, and AAV-PHP.eB carrying EGFP and AAV-MaCPNS1 carrying mCherry was administered to P1 Twi mice via facial vein injection at a total dose of 4×10^{11} vg (2×10^{11} vg per vector). Brain tissues were harvested at P38, and fluorescence imaging showed robust EGFP and mCherry signals in the brain, with fluorescence detected in peripheral organs, such as the heart and liver (Figure 7). Based on the fluorescence signal distribution, qPCR was conducted to quantify vector genome levels in specific brain regions and major organs. Consequently, vector genome levels were broadly increased across the brain, with markedly enriched accumulation observed in the frontal cortex (FC), brainstem (BS), and SC. Among peripheral organs, the heart and liver showed the highest levels of vector accumulation, with statistically significant differences detected for the PE2max-NT and CT vectors (Figures 8A–D and Tables 3 and 4).

These expression patterns closely reflected the previously observed fluorescence distribution. The concordance between protein-level fluorescence and vector genome abundance measured via qPCR provides strong evidence for the effective delivery and functional activation of the vector in target tissues.

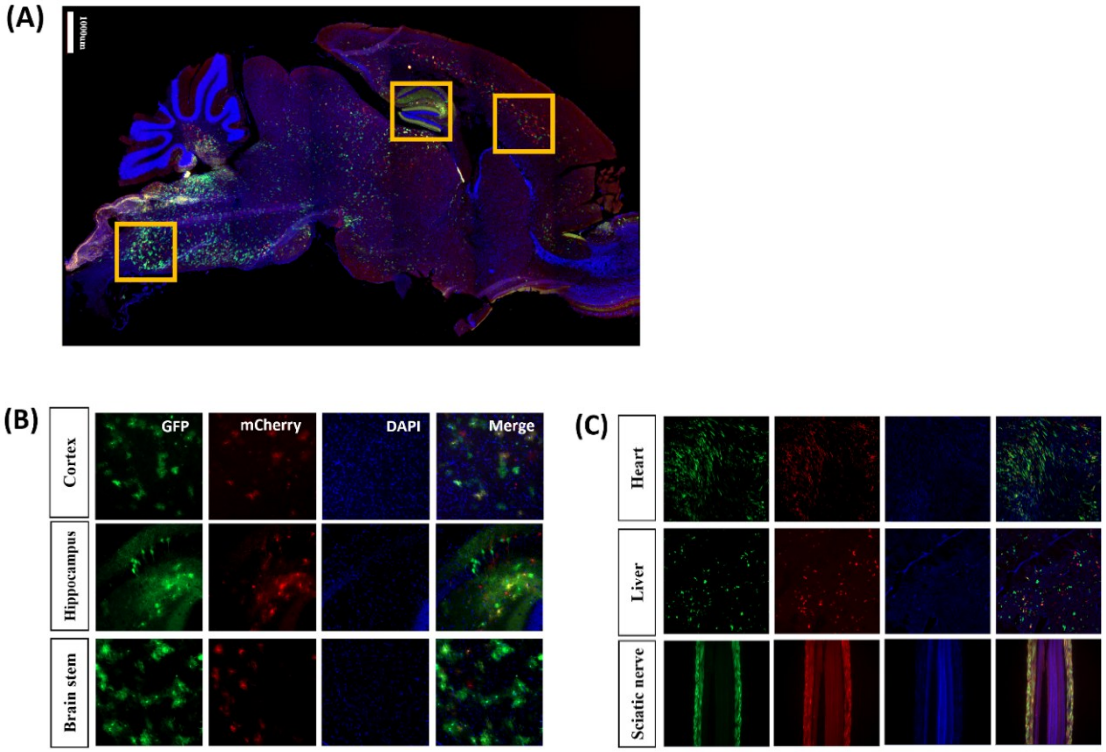

Figure 7. Systemic distribution of AAV-PHP.eB and AAV-MaCPNS1 vectors in central and peripheral tissues after facial vein injection.

(A) Representative sagittal section of a mouse brain showing widespread fluorescence at P1 following co-injection of AAV-PHP.eB-GFP (green) and AAV-MaCPNS1-mCherry (red). DAPI (blue) stains nuclei. Tilescan; scale bar = 1,000 μm. Yellow boxes indicate regions of interest shown at a higher magnification in (B), which include the cortex, hippocampus, and brainstem, particularly highlighting regions. (C) Fluorescence images of peripheral tissues, including the heart, liver, and SN. Scale bar = 50 μm. GFP, green fluorescent protein.

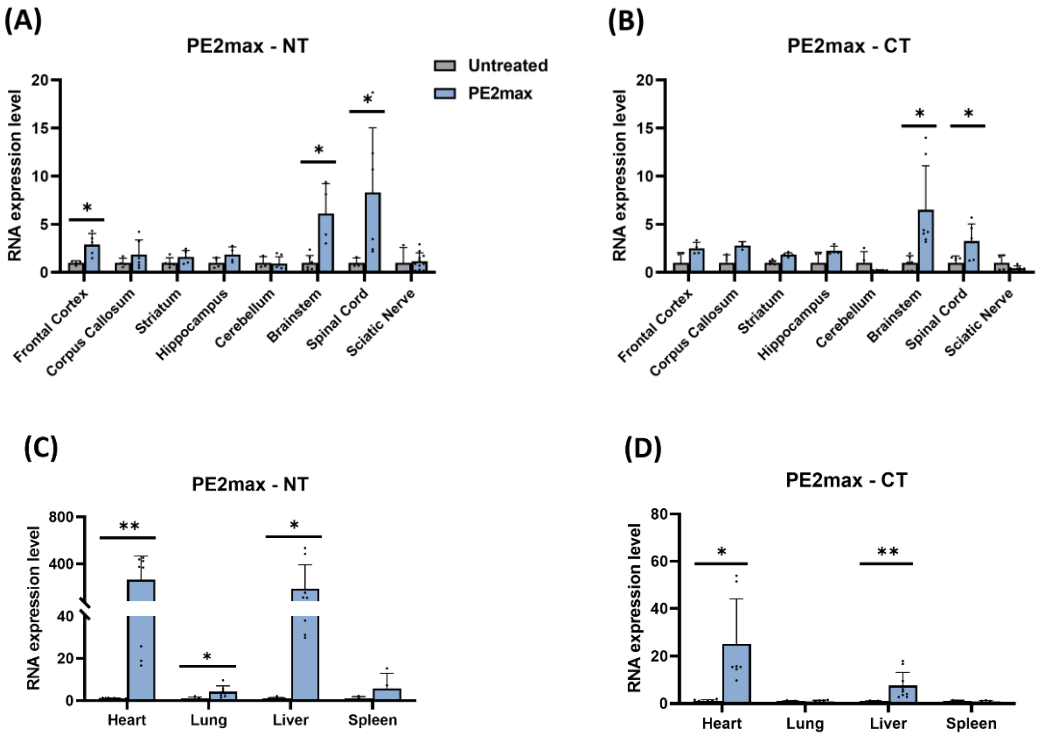

Figure 8. mRNA expression levels of viral vectors in the brain regions and peripheral organs. (A–D) Graphs comparing RNA expression levels in PE2max-NT- and CT-treated mice versus untreated controls. $n = 3$ animals/group. Values are expressed as means with error bars representing the standard error of the mean. All statistical analyses were conducted using an independent *t*-test (*$P < 0.05$, ** $P < 0.01$, ** $P < 0.001$).

Table 3. Heterogeneity of variance in viral vector mRNA expression across brain regions and peripheral organs

Name	Untreated-NT	PE2max-NT	F-value	P-value	Untreated-CT	PE2max-CT	F-value	P-value
Frontal Cortex	1.00 ± 0.10	2.90 ± 0.51	8.316	0.024*	1.00 ± 0.53	2.50 ± 0.32	9.305	0.023*
Corpus Callosum	1.00 ± 0.25	1.73 ± 0.54	4.394	0.066	1.03 ± 0.39	1.30 ± 0.10	8.086	0.017*
Striatum	1.00 ± 0.23	1.61 ± 0.30	0.744	0.413	1.00 ± 0.08	1.84 ± 0.09	0.419	0.532
Hippocampus	1.00 ± 0.26	1.85 ± 0.40	3.485	0.111	1.00 ± 0.55	2.26 ± 0.23	26.213	0.002**
Cerebellum	1.00 ± 0.37	0.93 ± 0.26	0.141	0.717	1.00 ± 0.58	0.24 ± 0.01	14.590	0.007**
Brain stem	1.00 ± 0.28	6.12 ± 1.56	41.907	<0.001***	1.00 ± 0.11	5.40 ± 1.77	172.465	<0.001***
Spinal cord	1.00 ± 0.48	8.31 ± 2.75	27.182	0.002**	1.00 ± 0.29	3.25 ± 0.73	3.427	0.094
Sciatic Nerve	1.00 ± 2.85	1.26 ± 0.28	2.667	0.131	1.00 ± 0.41	0.44 ± 0.10	37.639	<0.001***
Heart	1.00 ± 1.03	264.66 ± 72.23	100.171	<0.001***	1.00 ± 0.16	25.14 ± 7.16	34.636	<0.001***
Lung	1.00 ± 0.35	4.22 ± 1.06	3.36	0.097	1.00 ± 0.09	0.51 ± 0.15	7.846	0.017*
Liver	1.00 ± 1.19	186.39 ± 72.39	17.091	<0.001***	1.00 ± 0.10	7.51 ± 1.76	7.871	0.015*
Spleen	1.00 ± 0.48	5.77 ± 3.59	8.227	0.028*	1.00 ± 0.22	0.80 ± 0.18	0.070	0.798

Note: Values are expressed as means with error bars representing the standard error of the mean (SEM). All statistical analyses were conducted using an independent *t*-test (*$P < 0.05$, **$P < 0.01$, **$P < 0.001$).

Table 4. Statistical analysis of group-wise differences in viral vector mRNA expression across brain regions and peripheral organs

Region	Comparison groups			N	P-value
Frontal Cortex	Untreated-NT	vs	PE2max- NT	4:5	0.019*
	Untreated-CT	vs	PE2max- CT	4:4	0.062
Corpus Callosum	Untreated-NT	vs	PE2max- NT	4:7	0.361
	Untreated-CT	vs	PE2max- CT	7:5	0.590
Striatum	Untreated-NT	vs	PE2max- NT	5:5	0.147
	Untreated-CT	vs	PE2max- CT	7;5	0.103
Hippocampus	Untreated-NT	vs	PE2max- NT	4:4	0.127
	Untreated-CT	vs	PE2max- CT	4:4	0.101
Cerebellum	Untreated-NT	vs	PE2max- NT	3:7	0.879
	Untreated-CT	vs	PE2max- CT	4;5	0.282
Brain stem	Untreated-NT	vs	PE2max- NT	7:4	0.044*
	Untreated-CT	vs	PE2max- CT	6:4	0.017*
Spinal cord	Untreated-NT	vs	PE2max- NT	3:5	0.045*
	Untreated-CT	vs	PE2max- CT	6:6	0.015*
Sciatic Nerve	Untreated-NT	vs	PE2max- NT	3:10	0.715
	Untreated-CT	vs	PE2max- CT	4:6	0.427
Heart	Untreated-NT	vs	PE2max- NT	10:8	0.008**
	Untreated-CT	vs	PE2max- CT	10:7	0.005**
Lung	Untreated-NT	vs	PE2max- NT	5:7	0.033*
	Untreated-CT	vs	PE2max- CT	5:8	0.218
Liver	Untreated-NT	vs	PE2max- NT	8:8	0.037*
	Untreated-CT	vs	PE2max- CT	5:10	0.023*
Spleen	Untreated-NT	vs	PE2max- NT	4:4	0.277
	Untreated-CT	vs	PE2max- CT	4:6	0.264

Note: Values are expressed as means with error bars representing the standard error of the mean (SEM). All statistical analyses were conducted using an independent t-test (*$P < 0.05$, ** $P < 0.01$, ** $P < 0.001$).

3.3. Precise correction of the target adenine by PE2max without detectable off-target effects

Evaluation of gene correction efficiency was conducted through *in vitro* transfection in mutant *Galc* HEK293T cells and *in vivo* vector delivery in Krabbe mice (Figure 9A). AAV-PE2max was delivered at MOI 10^5 vg/cell, and editing efficiency was measured at days 4, 7, and 10 via targeted deep sequencing. Peak editing (~8%) was observed on day 4 but declined over time. As time passes, uninfected cells may surpass infected cells in proliferation, resulting in a reduced proportion of edited cells (Figure 9B). Quantification of editing efficiency at both on- and off-target sites showed that specific editing exclusively occurred at the on-target locus in the AAV-PE2max-treated group. (Figures 10A–C). The indel frequencies at all loci remained at background levels in both treated and untreated samples. These results indicate precise editing by PE2max without detectable off-target effects. To thoroughly assess *in vivo* correction efficiency, the brains of Krabbe mice were dissected into specific regions. gDNA analysis revealed the highest efficiency up to 5% in the FC and CC, followed by the HC, BS, and SC (Figure 11A). Similarly, cDNA analysis revealed high efficiency up to 10% in the FC, CC, and HC, followed by BS and then SC (Figure 11B). However, a relatively low correction efficiency was observed in the SN region of the PNS. Overall, the gDNA and cDNA profiles showed high concordance, supporting the consistency of regional editing.

In vivo, to further verify the precision of PE, substitution frequency was analyzed across a 40-nt window surrounding the target site in the *Galc* coding sequence. A sharp editing peak at nucleotide 1,063 was observed, which corresponded to the intended A-to-G substitution, with no significant off-target substitutions or indels in neighboring regions. (Figure 12). The results confirmed consistent correction efficiencies in the CNS between gDNA and cDNA analyses, indicating accurate correction without off-target modifications.

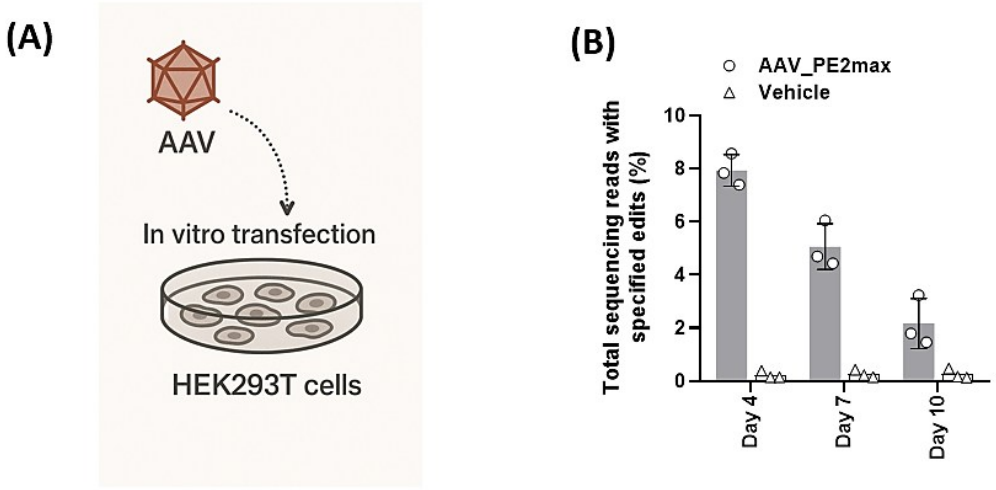

Figure 9. *In vitro* evaluation of PE2max editing efficiency in mutant *Galc* -expressing HEK293T cells.

(A) Schematic of the *in vitro* transfection strategy using AAV vectors in mutant *Galc* -expressing HEK293T cells. (B) Time-course analysis revealing higher proportions of precisely edited reads in the AAV-PE2max group than in the vehicle control at days 4, 7, and 10 post-transfection. $n = 3$ animals/group. Values are expressed as means with error bars representing the standard error of the mean.

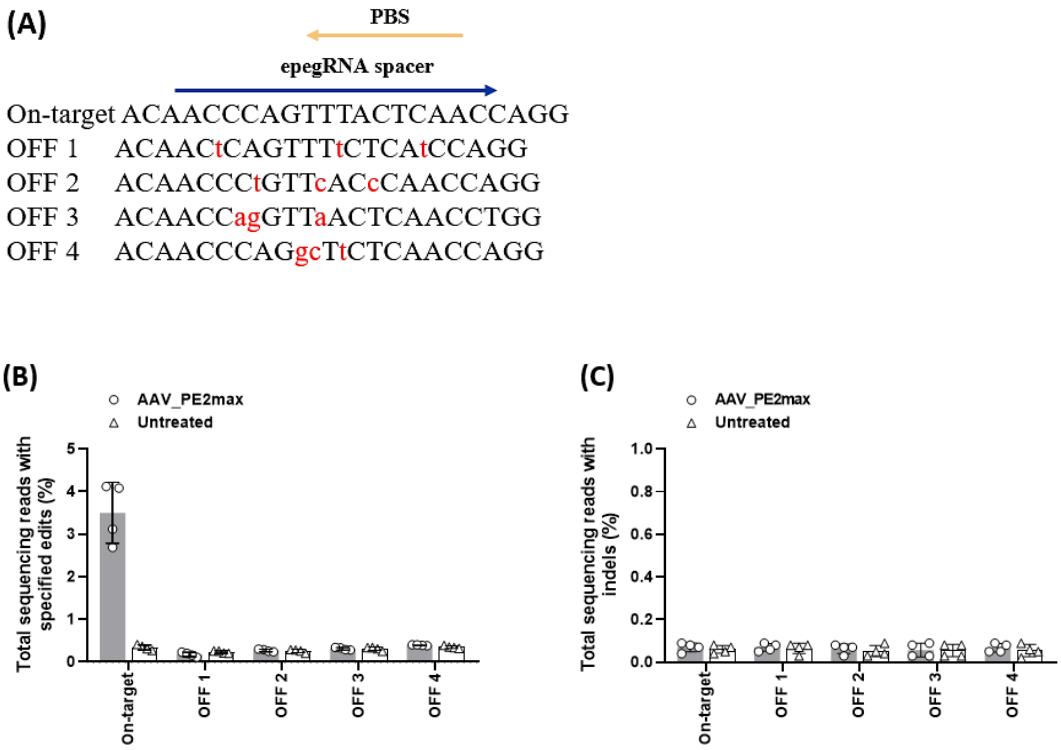

Figure 10. Specificity and editing precision of AAV-PE2max *in vitro*.

(A) Alignment of the on-target sequence and the top four off-target candidate sites predicted based on sequence similarity. Mismatched bases are presented in red. (B) Editing efficiencies measured at the on- and off-target sites. (C) Indel frequencies at the same loci in treated and untreated samples. $n = 4$ animals/group. Values are expressed as means with error bars representing the standard error of the mean.

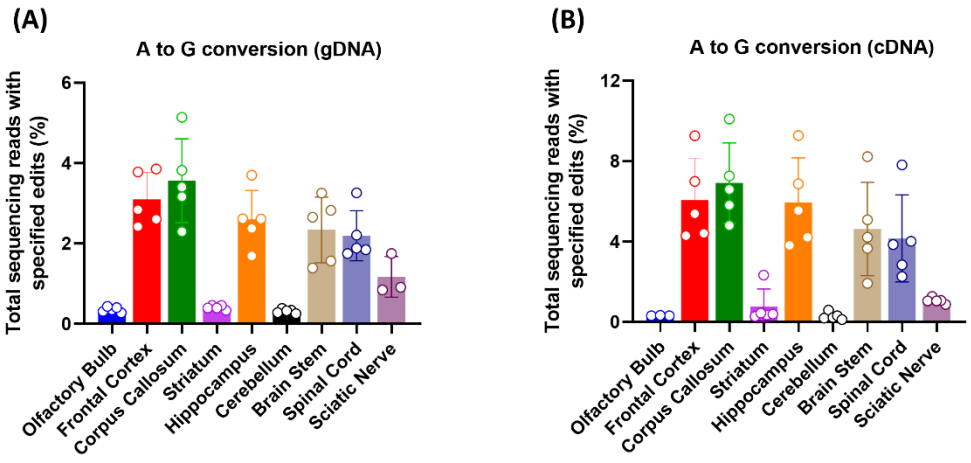

Figure 11. Editing efficiency levels of PE2max vectors in the brain and six body organs. The percentage of adenine conversion is used as an indicator of a successful and efficient PE. The editing efficiency of PE2max was evaluated in more specifically dissected brain regions. (A) A-to-G substitution frequencies in genomic DNA (gDNA) as measured by NGS. (B) A-to-G substitution frequencies in complementary DNA (cDNA) from the same samples. n=5. Values are expressed as means with error bars representing the standard error of the mean. NGS, next-generation sequencing.

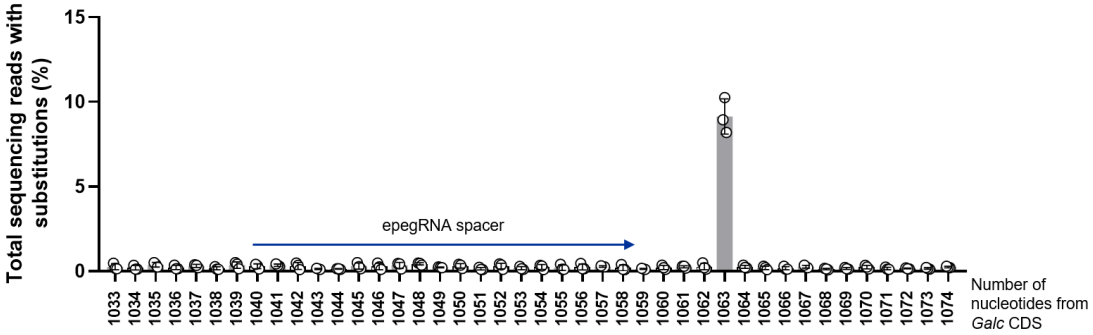

Figure 12. Indel frequency analysis revealed negligible levels of unwanted insertions or deletions (indels).

Within the targeted region, a distinct peak was observed at position 1,063, which corresponded to the intended edit site. The epegRNA spacer sequence is indicated by the blue arrow. Substitution frequency was analyzed via NGS across a 40-bp window surrounding the target site. n=3. Values are expressed as means with error bars representing the standard error of the mean.

3.4. Prime editing using PE2max promotes GALC expression and myelination in the central nervous system of twitcher mice

A hallmark pathological feature of KD progression is the demyelination of the CC, alongside rapid white matter collapse and a subsequent arrest in oligodendrocyte maturation. MBP is a major constituent of myelin and plays a pivotal role in maintaining myelin sheath structure and axonal insulation. In KD, MBP expression is substantially reduced owing to the loss and functional impairment of oligodendrocytes, which are the primary myelinating cells in the CNS. Such a reduction reflects the extensive demyelination and failure of oligodendrocyte maturation due to psychosine accumulation. Therefore, after IV administration of PE2max at P1, it was hypothesized that the base correction of the target mutation would not only increase GALC expression but also promote the recovery of myelin-associated factors. To confirm GALC expression after the correction of mutations in the *Galc* gene, molecular and histological approaches were employed.

Quantitative analysis via qRT-PCR revealed a considerable increase in GALC expression across most brain regions, except for the HC, with the greatest increase observed in the BS. Although the SN exhibited an increasing trend, it did not reach statistical significance (Figure 13 and Tables 5 and 6). This result confirmed that PE2max corrected the intended base and reestablished normal GALC levels across RNA and protein expression. Immunofluorescence (IF) staining was performed to visualize protein expression across distinct brain regions. In addition to GALC, the expression of MBP, a key component of the myelin sheath, was also analyzed to evaluate potential effects on myelination. Quantitative analysis revealed a general increase in GALC expression compared with the untreated group, with a statistically significant upregulation in the FC, CBLL, BS, and SC regions. For MBP, significant increases were found in the FC, STR, BS, and SC (Figure 14 and Tables 7 and 8). This suggests that increased GALC and MBP expressions occurred in brain regions with high base editing efficiency.

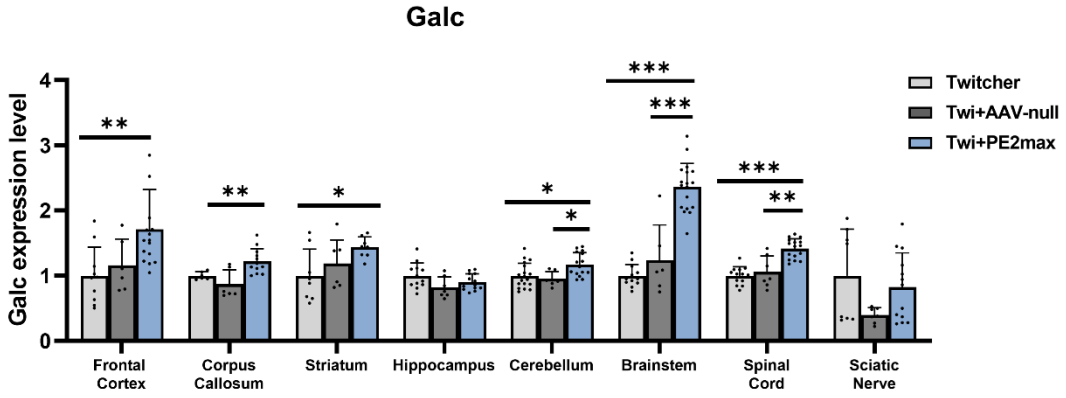

Figure 13. Validation of *Galc* expression through a molecular approach.

Quantitative analysis of *Galc* levels was conducted via qPCR. $n = 4$ for untreated, $n = 5$ for PE2max, and $n = 3$ for AAV-null. Values are expressed as means with error bars representing the standard error of the mean. One-way ANOVA with Bonferroni's multiple comparison tests was conducted. Statistically significant differences are shown as $*P < 0.05$, $**P < 0.01$, and $***P < 0.001$.

Table 5. Heterogeneity of variance in *Galc* mRNA expression across selected CNS and PNS regions

Region	Untreated	AAV-null	PE2max	F-value	P-value
Frontal Cortex	1.00 ± 0.14	1.16 ± 0.17	1.71 ± 0.15	6.276	0.005**
Corpus Callosum	1.00 ± 0.02	0.87 ± 0.09	1.22 ± 0.06	8.472	0.002**
Striatum	1.00 ± 0.14	1.19 ± 0.14	1.43 ± 0.06	3.608	0.046*
Hippocampus	1.00 ± 0.06	0.82 ± 0.06	0.89 ± 0.03	3.006	0.065
Cerebellum	1.00 ± 0.05	0.95 ± 0.04	1.17 ± 0.05	5.451	0.008**
Brainstem	1.00 ± 0.05	1.24 ± 0.22	2.36 ± 0.08	62.844	<0.001***
Spinal cord	1.00 ± 0.04	1.06 ± 0.09	1.42 ± 0.04	25.089	<0.001***
Sciatic Nerve	1.00 ± 0.25	0.39 ± 0.04	0.83 ± 0.14	2.645	0.091

Note: Values are expressed as means ± SEM. One-way ANOVA with Bonferroni's multiple comparison test was conducted. Statistically significant differences are shown as $*P < 0.05$, $**P < 0.01$, and $***P < 0.001$.

Table 6. Statistical analysis of group-wise differences in Galc mRNA expression across selected CNS and PNS regions

Region	Comparison groups			N	P-value
Frontal Cortex	Untreated	vs	PE2max	10 : 16	0.007**
	Untreated	vs	AAV-null	10 : 6	1.000
	PE2max	vs	AAV-null	16 : 6	0.109
Corpus Callosum	Untreated	vs	PE2max	6 : 12	0.656
	Untreated	vs	AAV-null	6 : 8	0.131
	PE2max	vs	AAV-null	12 : 8	0.002**
Striatum	Untreated	vs	PE2max	8 : 8	0.043*
	Untreated	vs	AAV-null	8 : 8	0.829
	PE2max	vs	AAV-null	8 : 8	0.473
Hippocampus	Untreated	vs	PE2max	12 : 14	0.320
	Untreated	vs	AAV-null	12 : 8	0.076
	PE2max	vs	AAV-null	14 : 8	0.969
Cerebellum	Untreated	vs	PE2max	18 : 15	0.023*
	Untreated	vs	AAV-null	18 : 8	1.000
	PE2max	vs	AAV-null	15 : 8	0.028*
Brain stem	Untreated	vs	PE2max	12 : 19	<0.001***
	Untreated	vs	AAV-null	12 : 6	0.557
	PE2max	vs	AAV-null	19 : 6	<0.001***
Spinal cord	Untreated	vs	PE2max	13 : 16	<0.001***
	Untreated	vs	AAV-null	13 : 7	1.000
	PE2max	vs	AAV-null	16 : 7	0.003**
Sciatic Nerve	Untreated	vs	PE2max	8 : 13	1.000
	Untreated	vs	AAV-null	8 : 7	0.091
	PE2max	vs	AAV-null	13 : 7	0.271

Note: Values are expressed as means ± SEM. One-way ANOVA with Bonferroni's multiple comparison test was conducted. Statistically significant differences are shown as $*P < 0.05$, $**P < 0.01$, and $***P < 0.001$.

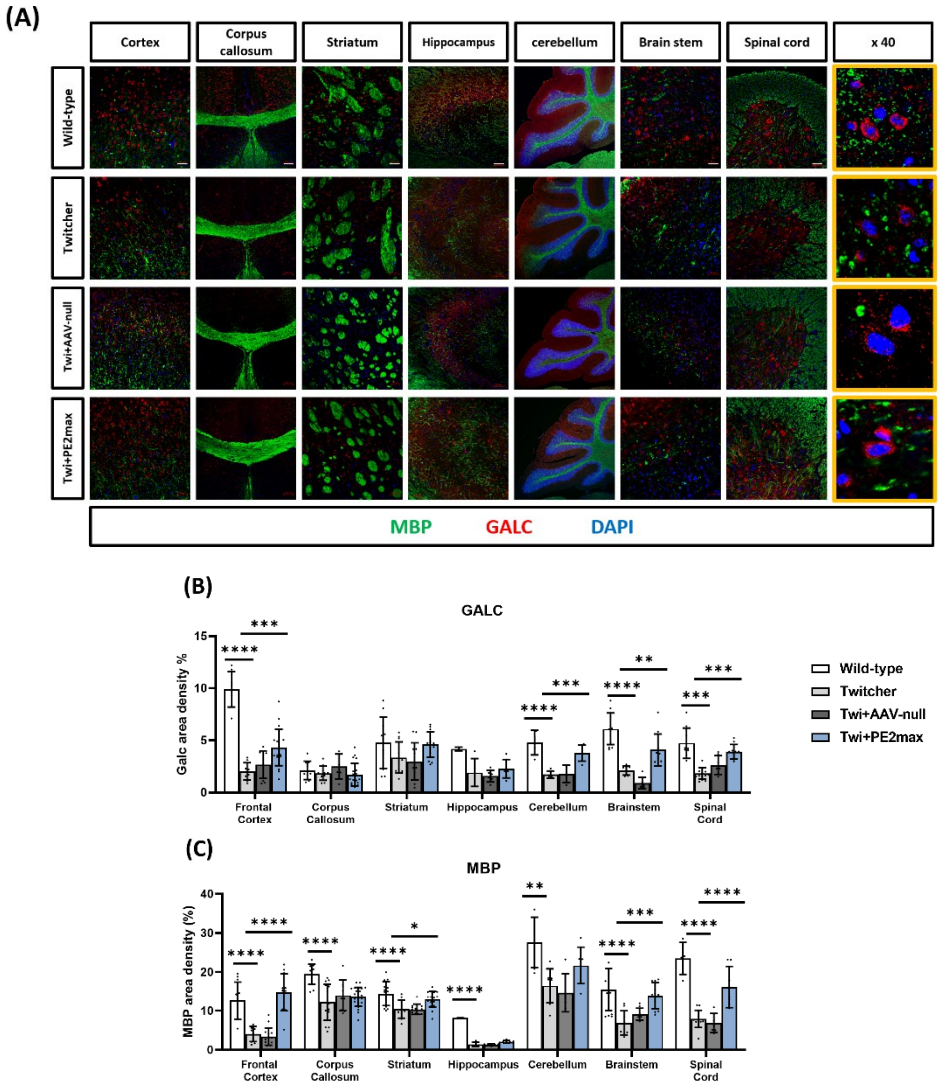

Figure 14. Results from the IF analysis of GALC protein expression confirmed.

(A) The image shows the staining of MBP (green), GALC (red), and DAPI (blue) in the brain and spinal cord regions for each group. (B) Quantification of the GALC and (C) MBP expression levels as measured by area density (%) in each region; $n = 4$ images/animal, 3 animals/group. Scale bar: = 50 μm; 100 μm for corpus callosum; 40×. Values are expressed as means with error bars representing the standard error of the mean. One-way ANOVA with Bonferroni's multiple comparison tests was conducted. Statistically significant differences are shown as $*P < 0.05$, $**P < 0.01$, and $***P < 0.001$.

Table 7. Heterogeneity of variance in GALC and MBP expressions across selected brain regions and the spinal cord

	Region	Wild type	Untreated	AAV-null	PE2max	F-value	P-value
GALC	Frontal Cortex	9.90 ± 0.60	2.02 ± 0.28	2.67 ± 0.42	4.32 ± 0.38	45.932	<0.001***
	Corpus Callosum	2.12 ± 0.27	1.84 ± 0.20	2.50 ± 0.49	1.70 ± 0.25	1.176	0.330
	Striatum	4.77 ± 0.74	3.34 ± 0.43	2.98 ± 0.52	4.76 ± 0.34	3.536	0.022*
	Hippocampus	4.16 ± 0.13	1.90 ± 0.59	1.58 ± 0.23	2.27 ± 0.33	4.169	0.023*
	Cerebellum	4.78 ± 0.54	1.71 ± 0.14	1.78 ± 0.43	3.76 ± 0.31	17.354	<0.001***
	Brainstem	6.11 ± 0.45	2.09 ± 0.15	0.83 ± 0.19	4.08 ± 0.49	35.076	<0.001***
	Spinal cord	4.73 ± 0.44	1.68 ± 0.17	2.63 ± 0.34	3.89 ± 0.22	15.061	<0.001***
MBP	Frontal Cortex	12.65 ± 1.45	4.03 ± 0.61	3.40 ± 0.57	14.74 ± 1.38	31.290	<0.001***
	Corpus Callosum	19.43 ± 0.74	12.20 ± 1.20	13.97 ± 1.33	13.62 ± 0.50	11.493	<0.001***
	Striatum	14.42 ± 0.84	10.40 ± 0.67	10.36 ± 0.38	13.00 ± 0.48	9.947	<0.001***
	Hippocampus	8.13 ± 0.04	1.42 ± 0.26	1.32 ± 0.09	2.07 ± 0.13	185.014	<0.001***
	Cerebellum	27.58 ± 2.63	16.44 ± 1.54	14.65 ± 2.20	21.66 ± 1.77	7.840	<0.001***
	Brainstem	15.46 ± 1.38	6.92 ± 1.03	9.17 ± 0.50	14.25 ± 0.97	11.994	<0.001***
	Spinal cord	23.44 ± 1.67	7.95 ± 0.61	6.91 ± 0.92	16.13 ± 2.00	36.216	<0.001***

Note: Values are presented as means ± SEM. One-way ANOVA and with Bonferroni's multiple comparison test was conducted. Statistically significant differences are shown as $*P < 0.05$, $**P < 0.01$, and $***P < 0.001$

Table 8. Statistical analysis of group-wise differences in GALC and MBP expressions across selected brain regions and the spinal cord

	Region	Comparison groups			N	P-value
GALC	Frontal Cortex	PE2max	vs	Wild type	21 : 8	<0.001***
			vs	Untreated	21 : 9	0.003**
			vs	AAV-null	21 : 10	0.044*
		AAV-null	vs	Wild type	10 : 8	<0.001***
			vs	Untreated	10 : 9	1.000
		Untreated	vs	Wild type	9 : 8	<0.001***
	Corpus Callosum	PE2max	vs	Wild type	20 : 11	1.000
			vs	Untreated	20 : 11	1.000
			vs	AAV-null	20 : 6	0.545
		AAV-null	vs	Wild type	6 : 11	1.000
			vs	Untreated	6 : 11	1.000
		Untreated	vs	Wild type	11 : 11	1.000
	striatum	PE2max	vs	Wild type	16 : 11	1.000
			vs	Untreated	16 : 12	0.252
			vs	AAV-null	16 : 12	0.069
		AAV-null	vs	Wild type	12 : 11	0.118
			vs	Untreated	12 : 12	1.000
		Untreated	vs	Wild type	11 : 12	0.364
	Hippocampus	PE2max	vs	Wild type	7 : 4	0.120
			vs	Untreated	7 : 5	1.000
			vs	AAV-null	7 : 6	1.000
		AAV-null	vs	Wild type	6 : 4	0.019*
			vs	Untreated	6 : 5	1.000
		Untreated	vs	Wild type	5 : 4	0.056
	Cerebellum	PE2max	vs	Wild type	6 : 5	0.340
			vs	Untreated	6 : 6	0.003**

			vs	AAV-null	6 :4	0.010**
		AAV-null	vs	Wild type	4 : 5	<0.001***
			vs	Untreated	4 : 6	1.000
		Untreated	vs	Wild type	6 : 5	<0.001***
	Brain stem	PE2max	vs	Wild type	10 : 11	0.003**
			vs	Untreated	10 : 7	0.010**
			vs	AAV-null	10 : 7	<0.001***
		AAV-null	vs	Wild type	7 : 11	<0.001***
			vs	Untreated	7 : 7	0.261
		Untreated	vs	Wild type	7 : 11	<0.001***
	Spinal cord	PE2max	vs	Wild type	10 :11	0.003**
			vs	Untreated	10 :7	0.010**
			vs	AAV-null	10 : 7	<0.001***
		AAV-null	vs	Wild type	7 : 11	<0.001***
			vs	Untreated	4 : 7	0.261
		Untreated	vs	Wild type	7 : 11	0.010**
MBP	Frontal Cortex	PE2max	vs	Wild type	12 : 11	1.000
			vs	Untreated	12 : 10	<0.001***
			vs	AAV-null	12 : 15	<0.001***
		AAV-null	vs	Wild type	15 : 11	<0.001***
			vs	Untreated	15 : 10	1.000
		Untreated	vs	Wild type	10 : 11	<0.001***
	Corpus Callosum	PE2max	vs	Wild type	24 : 12	<0.001***
			vs	Untreated	24 : 15	1.000
			vs	AAV-null	24 : 9	1.000
		AAV-null	vs	Wild type	9 : 12	0.003**
			vs	Untreated	9 : 15	1.000
		Untreated	vs	Wild type	15 : 12	<0.001***
	striatum	PE2max	vs	Wild type	18 : 14	0.546
			vs	Untreated	18 : 12	0.024*

	AAV-null	vs	AAV-null	18 : 12	0.021*
		vs	Wild type	12 : 14	<0.001***
		vs	Untreated	12 : 12	1.000
	Untreated	vs	Wild type	12 : 14	<0.001***
Hippocampus	PE2max	vs	Wild type	7 : 4	<0.001***
		vs	Untreated	7 : 5	0.056
		vs	AAV-null	7 : 6	0.014*
	AAV-null	vs	Wild type	6 : 4	<0.001***
		vs	Untreated	6 : 5	1.000
	Untreated	vs	Wild type	5 : 4	<0.001***
Cerebellum	PE2max	vs	Wild type	7 : 6	0.289
		vs	Untreated	7 : 8	0.359
		vs	AAV-null	7 : 5	0.167
	AAV-null	vs	Wild type	5 : 6	0.002**
		vs	Untreated	5 : 8	1.000
	Untreated	vs	Wild type	8 : 6	0.003**
Brain stem	PE2max	vs	Wild type	12 : 15	1.000
		vs	Untreated	12 : 9	0.001**
		vs	AAV-null	12 : 9	0.030*
	AAV-null	vs	Wild type	9 : 15	0.003**
		vs	Untreated	9 : 9	1.000
	Untreated	vs	Wild type	9 : 15	<0.001***
Spinal cord	PE2max	vs	Wild type	7 : 6	0.004**
		vs	Untreated	7 : 13	<0.001***
		vs	AAV-null	7 : 7	<0.001***
	AAV-null	vs	Wild type	7 : 6	<0.001***
		vs	Untreated	7 : 13	1.000
	Untreated	vs	Wild type	13 : 6	<0.001***

Note: Values are expressed as means ± SEM. One-way ANOVA with Bonferroni's multiple comparison test was conducted. Statistically significant differences are shown as $*P < 0.05$, $**P < 0.01$, and $***P < 0.001$.

3.5. Recovery of GALC activity confirmed by enhanced enzymatic function and decreased psychosine accumulation

Based on previous findings showing a concurrent increase in GALC and MBP expressions in the FC, BS, and SC, the next step was to determine whether this molecular upregulation was accompanied by functional recovery. To determine whether the increased GALC expression resulted in functional enzyme activity, we conducted a fluorometric assay using HMU-β-gal, a substrate cleaved by β-galactosidase enzymes, such as GALC, which releases a fluorescent product (HMU) for quantitative measurement. Fluorescence analysis revealed a considerable increase in GALC activity in PE2max-treated samples, with particularly robust enhancement in the BS and SC regions (Figure 15 and Tables 9 and 10), indicating successful restoration of enzymatic function and protein expression.

To further confirm functional recovery, we evaluated psychosine accumulation, a hallmark of GALC deficiency. Psychosine is mainly produced via deacylation of GalCer by acid ceramidase and acts as a molecular trigger in KD. Psychosine is a toxic metabolite of GalCer that, when not degraded by GALC, disrupts lipid raft architecture, impairs cell signaling, and contributes to demyelination, neuroinflammation, axonal damage, and neurodegeneration. In untreated Twi mice, the psychosine levels were substantially elevated, whereas the PE2max treatment markedly reduced psychosine accumulation (Figure 16 and Table 11 and 12), supporting the restoration of the degradative function of GALC. Together, the recovery of GALC enzymatic activity and the reduction of psychosine—a central driver of KD pathology—strongly support the therapeutic potential of PE2max.

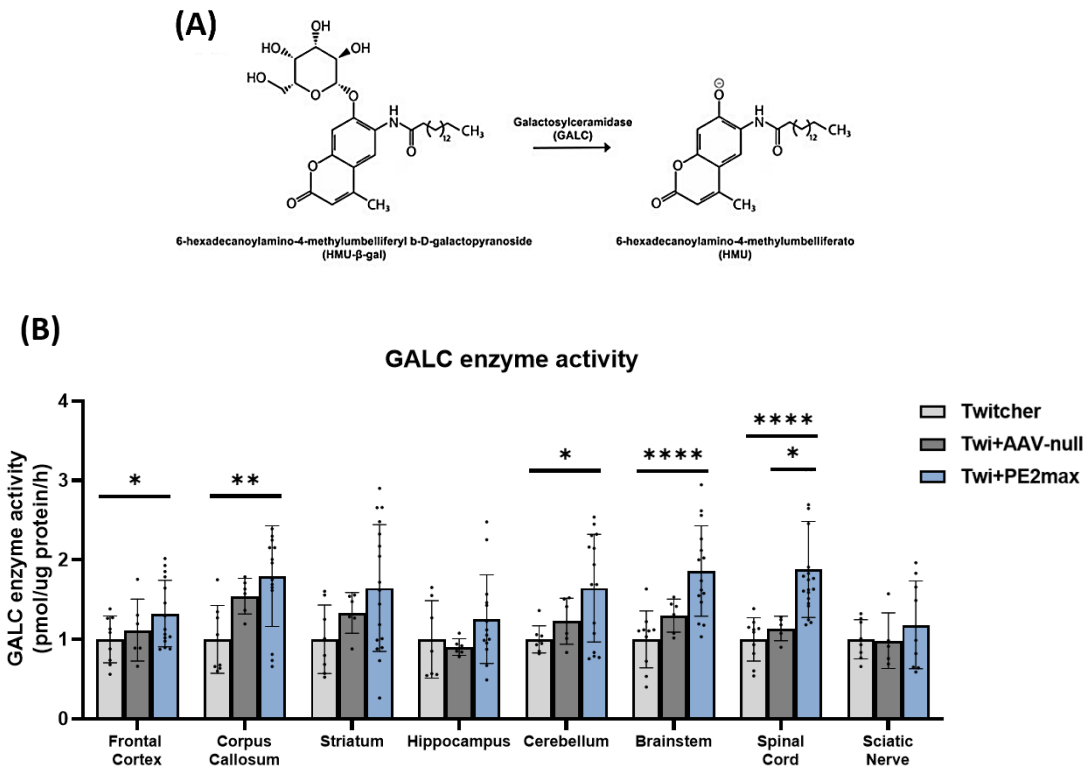

Figure 15. PE2max-mediated restoration of GALC enzymatic activity.

(A) Schematic representation of the enzymatic reaction catalyzed by GALC. Adapted from Peters et al. [35]. (B) A graph displaying the quantitative assessment of GALC enzyme activity based on fluorescence generated from an HMU β-gal substrate. $n = 3$ animals/group. Values are expressed as means with error bars representing the standard error of the mean. One-way ANOVA with Bonferroni's multiple comparison tests was conducted. Statistically significant differences are shown as $*P < 0.05$, $**P < 0.01$, and $***P < 0.001$.

Table 9. Heterogeneity of variance in GALC enzyme activity across selected CNS and PNS regions

Region	Untreated	AAV-null	PE2max	F-value	P-value
Frontal Cortex	1.00 ± 0.10	1.12 ± 0.16	1.48 ± 0.39	4.732	0.019*
Corpus Callosum	1.00 ± 0.15	1.55 ± 0.09	1.80 ± 0.16	6.018	0.007**
Striatum	1.00 ± 0.15	1.33 ± 0.10	1.65 ± 0.19	2.749	0.081
Hippocampus	1.00 ± 0.18	0.90 ± 0.04	1.26 ± 0.15	1.393	0.268
Cerebellum	1.00 ± 0.06	1.23 ± 0.12	1.65 ± 0.17	4.340	0.024*
Brainstem	1.00 ± 0.11	1.30 ± 0.09	1.86 ± 0.15	11.096	<0.001***
Spinal cord	1.00 ± 0.09	1.14 ± 0.07	1.88 ± 0.13	12.555	<0.001***
Sciatic Nerve	1.00 ± 0.09	0.98 ± 0.16	1.82 ± 0.18	0.535	0.594

Note: Values are expressed as means ± SEM. One-way ANOVA with Bonferroni's multiple comparison test was conducted. Statistically significant differences are shown as *$P < 0.05$, **$P < 0.01$, and ***$P < 0.001$.

Table 10. Statistical analysis of group-wise differences in GALC enzyme activity across selected CNS and PNS regions

Region	Comparison groups			N	P-value
Frontal Cortex	Untreated	vs	PE2max	9 : 11	0.022*
	Untreated	vs	AAV-null	9 : 6	1.000
	PE2max	vs	AAV-null	11 : 6	0.181
Corpus Callosum	Untreated	vs	PE2max	8 : 15	0.006**
	Untreated	vs	AAV-null	8 : 6	0.195
	PE2max	vs	AAV-null	15 : 6	0.997
Striatum	Untreated	vs	PE2max	8 : 17	0.084
	Untreated	vs	AAV-null	8 : 6	1.000
	PE2max	vs	AAV-null	17 : 6	0.964
Hippocampus	Untreated	vs	PE2max	7 : 14	0.783
	Untreated	vs	AAV-null	7 : 6	1.000
	PE2max	vs	AAV-null	14 : 6	0.432
Cerebellum	Untreated	vs	PE2max	8 : 15	0.026*
	Untreated	vs	AAV-null	8 : 6	1.000
	PE2max	vs	AAV-null	15 : 6	0.326
Brain stem	Untreated	vs	PE2max	10 : 15	<0.001***
	Untreated	vs	AAV-null	10 : 6	0.650
	PE2max	vs	AAV-null	15 :6	0.052
Spinal cord	Untreated	vs	PE2max	10 : 20	<0.001***
	Untreated	vs	AAV-null	10 : 5	1.000
	PE2max	vs	AAV-null	20 : 5	0.014*
Sciatic Nerve	Untreated	vs	PE2max	8 : 9	1.000
	Untreated	vs	AAV-null	8 : 5	1.000
	PE2max	vs	AAV-null	9 : 5	1.000

Note: Values are expressed as means ± SEM. One-way ANOVA with Bonferroni's multiple comparison test was conducted. Statistically significant differences are shown as $*P < 0.05$, $**P < 0.01$, and $***P < 0.001$.

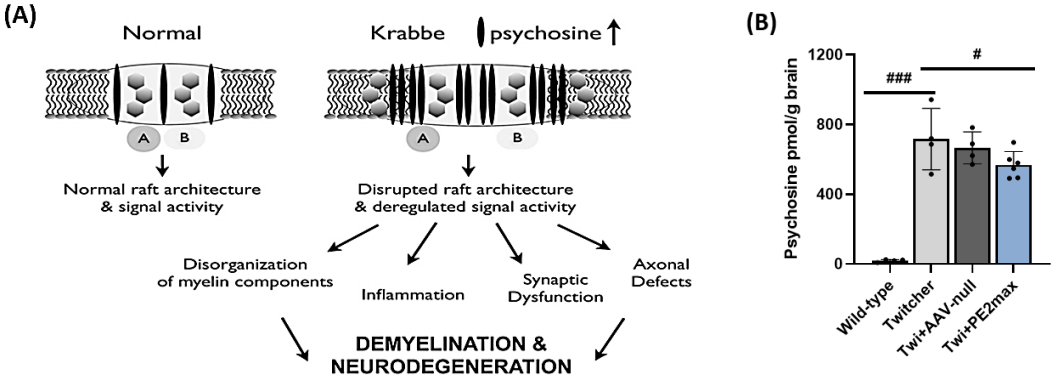

Figure 16. Psychosine levels were reduced in the brains of PE2max-treated twitcher mice.

(A) Schematic illustration of membrane raft disruption in Krabbe disease. Adapted from White et al. [36]. (B) Quantification of psychosine concentration in brain tissues (pmol/g) from wild-type, twitcher, and PE2max-treated twitcher mice. PE2max treatment markedly reduced the psychosine levels compared with the untreated Twitcher group. $n = 3$ animals/group. Values are expressed as means with error bars representing the standard error of the mean. One-way ANOVA with Bonferroni's multiple comparison tests was conducted. Statistically significant differences are shown as $^{*}P < 0.05$, $^{**}P < 0.01$, and $^{***}P < 0.001$.

Table 11. Heterogeneity of variance in psychosine levels across brain

Region	Wild-type	Untreated	AAV-null	PE2max	F-value	P-value
Brain	19.50±3.85	716.02±87.61	665.91±91.20	568.21±31.36	39.698	<0.001***

Note: Values are expressed as means ± SEM. One-way ANOVA with LSD multiple comparison test was conducted. Statistically significant differences are shown as $*P < 0.05$, $**P < 0.01$, and $***P < 0.001$.

Table 12. Statistical analysis of group-wise differences in psychosine levels across brain

Region	Comparison groups			N	P-value
Brain	PE2max	vs	Wild type	6 : 4	<0.001***
		vs	Untreated	6 : 4	0.042*
		vs	AAV-null	6 : 4	0.161
	AAV-null	vs	Wild type	4 : 4	<0.001***
		vs	Untreated	4 : 4	0.500
	Untreated	vs	Wild type	4 : 4	<0.001***

Note: Values are expressed as means ± SEM. One-way ANOVA with LSD multiple comparison test was conducted. Statistically significant differences are shown as $*P < 0.05$, $**P < 0.01$, and $***P < 0.001$.

3.6. Therapeutic Effects of PE2max on Demyelination and globoid cell pathology in a twitcher mouse model

Globoid cells, a major pathological hallmark of KD (also known as GCL), are multinucleated macrophages containing lipid inclusions resulting from myelin degradation. These cells typically accumulate in the white matter regions of the brain and SC, particularly in areas exhibiting severe myelin loss. Their presence is closely associated with chronic neuroinflammation, which exacerbates neuronal damage and impairs remyelination through the release of inflammatory mediators targeting neurons and oligodendrocytes.

To evaluate the disease pathology and the therapeutic effect of PE2max, LFB staining was employed to evaluate myelin preservation, whereas PAS staining was performed to detect globoid cells that accumulate as a result of myelin breakdown.

As observed in the FC, BS, and SC, PE2max-treated mice displayed a marked reduction in PAS-positive globoid cell accumulation compared with the untreated and AAV-null groups, indicating a significant alleviation of neuroinflammatory burden in the CNS (Figure 17 and Tables 13 and 14).

Moreover, in the CC—a representative white matter structure densely populated with myelinated fibers—myelin integrity was quantitatively evaluated by measuring mean gray values from LFB-stained sections. A higher mean gray value indicates stronger myelin staining. The PE2max group exhibited significantly increased gray values relative to control groups, indicating enhanced myelin preservation or potential remyelination (Figure 18 and Tables 15 and 16). These findings indicate that PE2max not only reduces the key pathological markers of KD but also contributes to structural myelin recovery in the affected CNS regions.

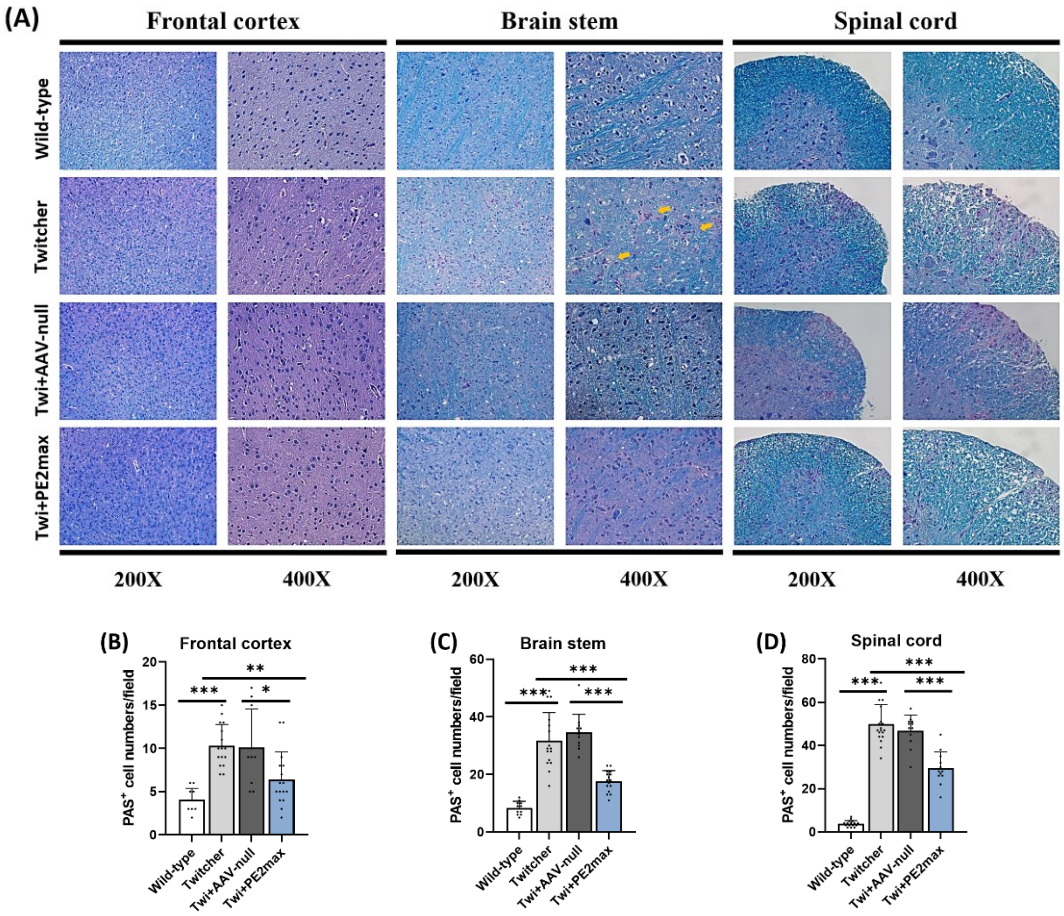

Figure 17. LFB/PAS staining was performed to evaluate the presence of globoid cells after PE2max treatment

(A) LFB/PAS staining images of the frontal cortex, brainstem, and spinal cord were obtained at 200× and 400× magnifications across four groups, where LFB labels myelin (blue) and PAS highlights globoid cells (pink). (B–D) The number of PAS-positive cells (yellow arrows) was counted in 400× images of each region). n=4 images/animal, 3 animals/group. Values are expressed as means with error bars representing the standard error of the mean. One-way ANOVA with Bonferroni's multiple comparison tests was conducted. Statistically significant differences are shown as $*P < 0.05$, $**P < 0.01$, and $***P < 0.001$.

Table 13. Heterogeneity of variance in the number of PAS-positive cells in the brain.

Region	Wild-type	Untreated	AAV-null	PE2max	F-value	P-value
Frontal Cortex	4.09 ± 0.39	10.31 ± 0.62	10.10 ± 1.41	6.44 ± 0.79	12.513	< 0.001***
Brainstem	8.36 ± 0.69	31.75 ± 2.44	31.50 ± 5.10	18.00 ± 0.92	15.796	< 0.001***
Spinal Cord	3.81 ± 0.36	49.95 ± 2.07	46.83 ± 2.09	29.42 ± 2.17	146.300	< 0.001***

Note: Values are expressed as means ± SEM. One-way ANOVA with Bonferroni's multiple comparison test was conducted. Statistically significant differences are shown as $*P < 0.05$, $**P < 0.01$, and $***P < 0.001$.

Table 14. Statistical analysis of group-wise differences in the number of PAS-positive cells in the brain.

Region	Comparison groups			N	P-value
Frontal Cortex	PE2max	vs	Wild type	16 : 11	0.303
		vs	Untreated	16 : 16	0.004**
		vs	AAV-null	16 : 10	0.023*
	AAV-null	vs	Wild type	10 : 11	< 0.001***
		vs	Untreated	10 :16	1.000
	Untreated	vs	Wild type	16 :16	< 0.001***
Brainstem	PE2max	vs	Wild type	15 : 11	0.119
		vs	Untreated	15 : 16	0.002**
		vs	AAV-null	15 : 12	0.007**
	AAV-null	vs	Wild type	12 : 11	< 0.001***
		vs	Untreated	12 : 16	1.000
	Untreated	vs	Wild type	16 : 11	< 0.001***
Spinal Cord	PE2max	vs	Wild type	12 : 16	< 0.001***
		vs	Untreated	12 : 19	< 0.001***
		vs	AAV-null	12 : 12	< 0.001***
	AAV-null	vs	Wild type	12 : 16	< 0.001***
		vs	Untreated	12 : 19	1.000
	Untreated	vs	Wild type	19 : 16	< 0.001***

Note: Values are expressed as means ± SEM. One-way ANOVA with Bonferroni's multiple comparison tests was conducted. Statistically significant differences are shown as $*P < 0.05$, $**P < 0.01$, and $***P < 0.001$.

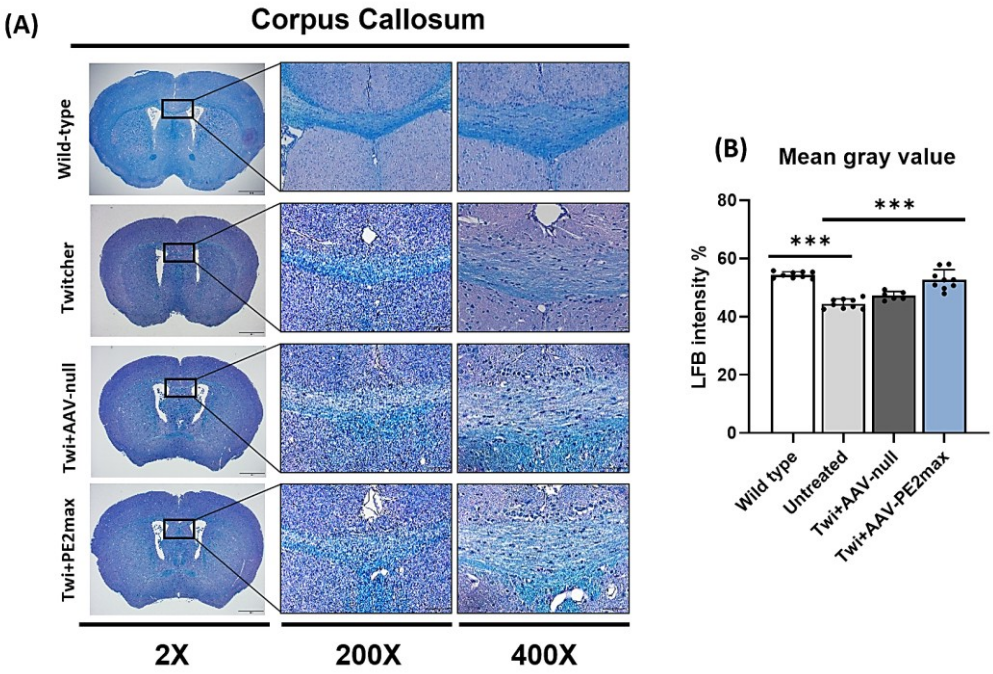

Figure 18. Assessment of myelin integrity in the corpus callosum using LFB staining. (A) LFB/PAS staining images of the corpus callosum was obtained at 2×, 200×, and 400× magnifications across the four groups, where LFB labels myelin (blue) and PAS highlights globoid cells (pink). n=3 images/animal, 3 animals/group. Values are expressed as means with error bars representing the standard error of the mean. One-way ANOVA with Bonferroni's multiple comparison tests was conducted. Statistically significant differences are shown as $*P < 0.05$, $**P < 0.01$, and $***P < 0.001$.

Table 15. Heterogeneity of variance in myelin intensity within the corpus callosum

Region	Wild-type	Untreated	AAV-null	PE2max	F-value	P-value
Corpus Callosum	54.33 ± 0.36	44.43 ± 0.56	47.17 ± 0.60	52.70 ± 1.15	39.217	< 0.001***

Note: Values are expressed as means ± SEM. One-way ANOVA with Bonferroni's multiple comparison tests was conducted. Statistically significant differences are shown as $*P < 0.05$, $**P < 0.01$, and $***P < 0.001$.

Table 16. Statistical analysis of group-wise differences in myelin intensity within the corpus callosum

Region	Comparison groups			N	P-value
Corpus Callosum	PE2max	vs	Wild type	9 : 9	0.748
		vs	Untreated	9 : 9	< 0.001***
		vs	AAV-null	9 : 6	< 0.001***
	AAV-null	vs	Wild type	6 : 9	< 0.001***
		vs	Untreated	6 : 9	0.145
	Untreated	vs	Wild type	9 : 9	< 0.001***

Note: Values are expressed as means ± SEM. One-way ANOVA with Bonferroni's multiple comparison tests was conducted. Statistically significant differences are shown as $*P < 0.05$, $**P < 0.01$, and $***P < 0.001$.

3.7. Although PE2max treatment enhanced myelin structure in the corpus callosum, no pathological changes were observed in the sciatic nerve.

The neuropathological morphology between Twi and WT mice were compared, and the neuronal condition in the PE2max group was assessed via transmission electron microscopy to visualize myelinated fibers in the CC and SN. Axonal diameter and g-ratio were used to evaluate neuronal damage and myelination status. The total number of axons within a defined field was determined, and the number of abnormal or degenerated myelin sheaths was counted to achieve a more refined pathological assessment.

The g-ratio, defined as the ratio of axonal diameter to the total diameter of the axon plus its myelin sheath, is considered to be optimal within the range of approximately 0.6–0.7. Higher values indicate thinner or damaged myelin, whereas lower values reflect thicker, well-preserved, or newly formed myelin via remyelination. In the corpus callosum (CC), PE2max-treated mice exhibited significantly lower g-ratio values than controls, indicating successful remyelination and recovery of myelin thickness in the CNS (Figure 19 Table 17 and 18). Scatter plot analysis of axon diameter versus g-ratio showed that the PE2max group's regression line more closely resembled that of wild-type mice, with an increased slope and decreased y-intercept, suggesting improved myelin integrity across various axon sizes (Figure 19C).

In the SN, axons in WT mice appeared tightly packed with uniform circular structures, whereas the Twi group showed reduced axon numbers, abnormally folded axons, and substantial macrophage infiltration (Figure 20A). PE2max treatment reduced the number of abnormal axons and infiltrating macrophages, indicating partial resolution of inflammation and improvement of the local neural environment (Figures 20B and C). However, g-ratio values remained largely unchanged (Figure 20E), and the overall distribution continued to differ significantly from wild-type mice. These findings suggest that the therapeutic efficacy of PE2max is more limited in the PNS than in the CNS.

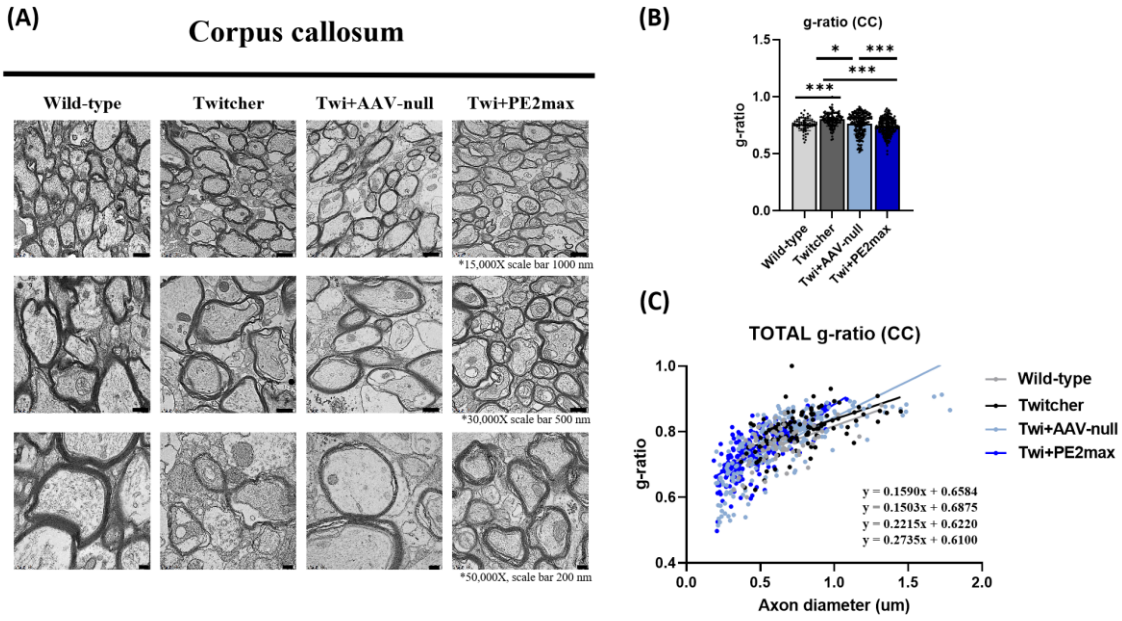

Figure 19. Electron microscopy (EM) shows myelin restoration in the corpus callosum after the PE2max treatment.

(A) EM images (15,000×, 30,000×, and 50,000×) of ultra-thin sections from corpus callosum). *n* = 10 images/animal, 3 animals/group. Scale bar = 50-μm ultra-thin sections. (B) Quantification of g-ratio (axon diameter/total fiber diameter). (C) Scatter plots were generated for each group, with separate trend lines applied to visualize the overall distribution patterns. n=30 images/animal, 3 animals/group. Values are expressed as means with error bars representing the standard error of the mean. One-way ANOVA with Bonferroni's multiple comparison tests was conducted. Statistically significant differences are shown as $*P < 0.05$, $**P < 0.01$, and $***P < 0.001$.

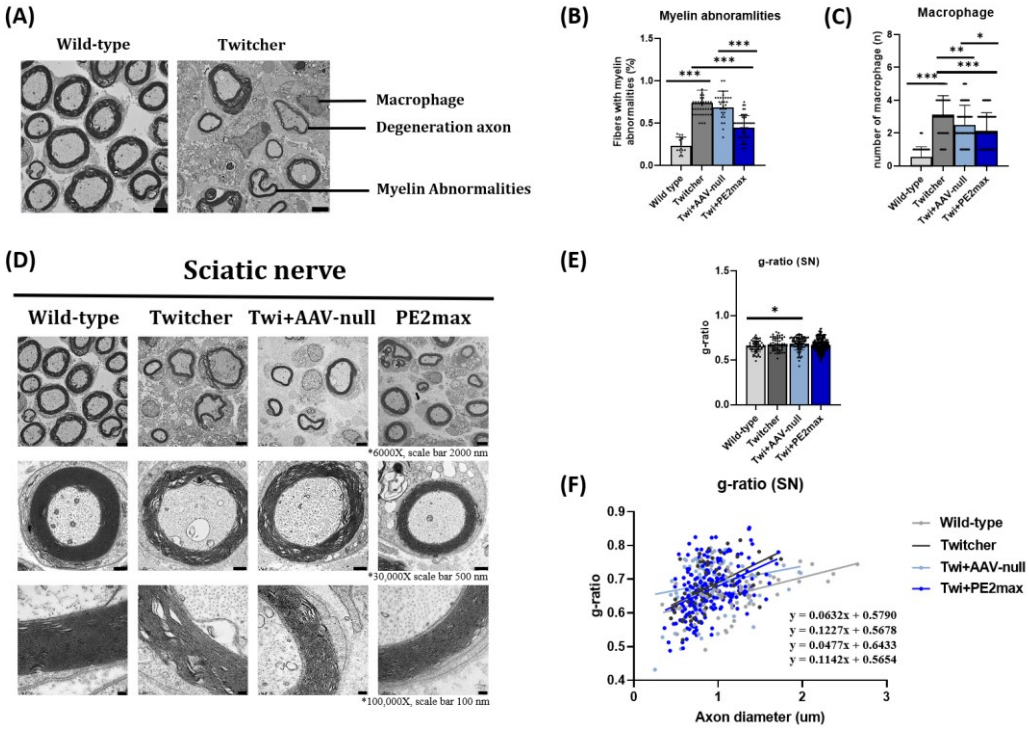

Figure 20. EM analysis of sciatic nerve pathology and limited response to PE2max treatment.

(A) Representative EM images of sciatic nerve cross-sections in wild-type and twitcher mice. (B,C) Quantification of abnormal myelin and macrophage infiltration in the sciatic nerves across the groups. (D) EM images (6,000×, 30,000×, and 100,000×) of ultra-thin sections from the sciatic nerves. (E) Quantification of g-ratio (axon diameter/total fiber diameter) and axon diameter. (F) Scatter plots were generated for each group, with separate trend lines applied to visualize the overall distribution patterns. n = 30 images/animal, 3 animals/group. Values are expressed as means with error bars representing the standard error of the mean. One-way ANOVA with Bonferroni's multiple comparison tests was conducted. Statistically significant differences are shown as $*P < 0.05$, $**P < 0.01$, and $***P < 0.001$.

Table 17. Heterogeneity of variance in the g-ratio of myelinated axons

Region	Wild type	Untreated	AAV-null	PE2max	F-value	P-value
Corpus callosum	0.76 ± 0.01	0.80 ± 0.01	0.76 ± 0.01	0.74 ± 0.00	15.656	<0.001***
Sciatic Nerve	0.65 ± 0.01	0.68 ± 0.01	0.70 ± 0.01	0.67 ± 0.01	5.999	<0.001***

Note: Values are expressed as means ± SEM. One-way ANOVA with Bonferroni's multiple comparison tests was conducted. Statistically significant differences are shown as *$P < 0.05$, **$P < 0.01$, and ***$P < 0.001$.

Table 18. Statistical analysis of group-wise differences in the g-ratio of myelinated axons

Region	Comparison groups			N	P-value
Corpus callosum	PE2max	vs	Wild type	217 : 65	0.663
		vs	Untreated	217 : 111	<0.001***
		vs	AAV-null	217 : 230	0.011*
	AAV-null	vs	Wild type	230 : 65	1.000
		vs	Untreated	230 : 111	<0.001***
	Untreated	vs	Wild type	111 : 65	0.002**
Sciatic Nerve	PE2max	vs	Wild type	204 : 62	0.829
		vs	Untreated	204 : 59	1.000
		vs	AAV-null	204 : 95	0.004**
	AAV-null	vs	Wild type	95 : 62	<0.001***
		vs	Untreated	95 : 59	0.389
	Untreated	vs	Wild type	59 : 62	0.412

Note: Values are expressed as means ± SEM. One-way ANOVA with Bonferroni's multiple comparison tests was conducted. Statistically significant differences are shown as *$P < 0.05$, **$P < 0.01$, and ***$P < 0.001$.

3.8. MRI-based evaluation indicates that the PE2max treatment led to partial white matter recovery in the treated mice

This study employed brain MRI to analyze four key DTI parameters commonly used to evaluate white matter microstructure: fractional anisotropy (FA), axial diffusivity (AD), radial diffusivity (RD), and mean diffusivity (MD). These metrics provide complementary insights into the integrity and organization of white matter.

FA and AD reflect the degree and directionality of water diffusion along axonal fibers. Generally, higher FA values are interpreted as reflecting more coherent and intact white matter tracts, typically associated with well-myelinated axons owing to the preferential movement of water molecules along aligned fiber bundles. Similarly, increased AD may reflect enhanced axonal integrity, although it is more specifically sensitive to axonal structural changes rather than myelin alone. Contrarily, RD and MD are considered to be markers of myelin integrity and overall diffusion. RD reflects water diffusion perpendicular to axonal fibers and is especially sensitive to alterations in myelin sheaths—higher RD values typically indicate demyelination. MD, representing the average diffusion across all directions, tends to increase in response to tissue breakdown or edema and decrease when cellular organization improves. Therefore, RD and MD reductions can be interpreted as signs of remyelination or tissue integrity restoration.

The PE2max-treated group exhibited markedly increased FA compared with the control group, suggesting partial recovery of myelination and enhanced fiber coherence in affected white matter regions. Although the observed reductions in RD and MD were not statistically significant, their downward trend is consistent with the hypothesis of remyelination or restoration of microstructural integrity. These findings collectively suggest that PE2max exerts neuroprotective or reparative effects on white matter, potentially through mechanisms that enhance myelin integrity or promote axonal recovery (Figure 21 and Tables 19 and 20).

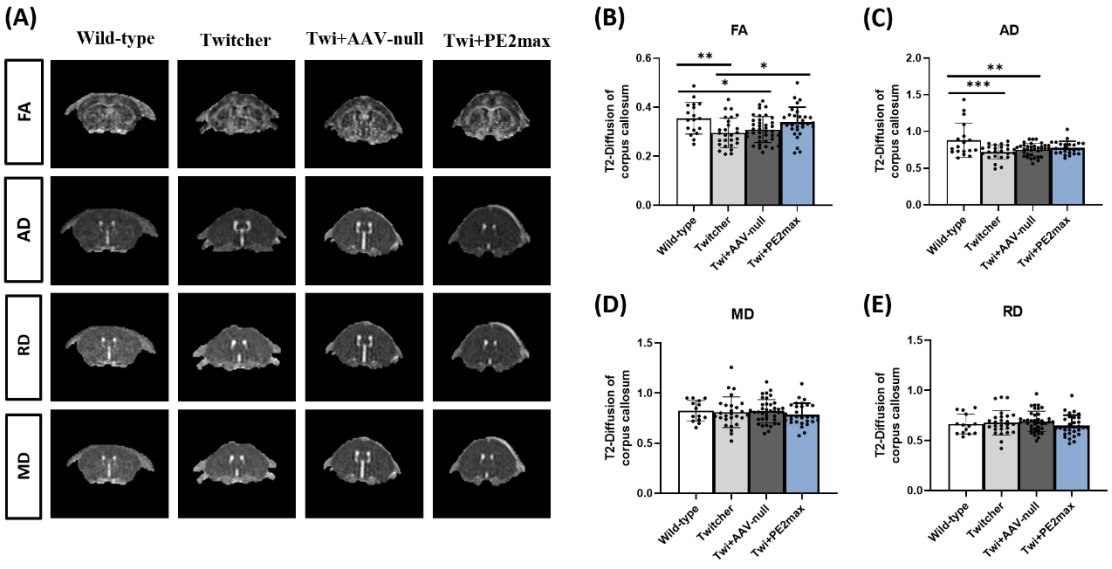

Figure 21. DTI analysis revealed improved myelination in the corpus callosum of PE2max-treated mice.

(A) Representative T2-weighted diffusion tensor imaging (DTI) maps showing the FA , AD , RD , and MD values in the corpus callosum for each group. (B–E) Quantification of DTI parameters in the corpus callosum. $n = 9$ images/animal, 3 animals/group. Values are expressed as means with error bars representing the standard error of the mean. One-way ANOVA with Bonferroni's multiple comparison tests was conducted. Statistically significant differences are shown as $^{*}P < 0.05$, $^{**}P < 0.01$, and $^{***}P < 0.001$.

Table 19. Heterogeneity of variance in DTI parameters of the corpus callosum across groups

DTI	Wild type	Untreated	AAV-null	PE2max	F-value	P-value
FA	0.35 ± 0.02	0.30 ± 0.01	0.31 ± 0.01	0.34 ± 0.01	5.097	0.002**
AD	0.88 ± 0.05	0.72 ± 0.02	0.78 ± 0.02	0.75 ± 0.01	6.002	<0.001***
RD	0.66 ± 0.03	0.68 ± 0.02	0.65 ± 0.02	0.69 ± 0.02	0.943	0.423
MD	0.82 ± 0.03	0.81 ± 0.03	0.79 ± 0.02	0.81 ± 0.02	0.440	0.725

Note: Values are expressed as means ± SEM. One-way ANOVA with Bonferroni's multiple comparison tests was conducted. Statistically significant differences are shown as $*P < 0.05$, $**P < 0.01$, and $***P < 0.001$.

Table 20. Statistical analysis of group-wise differences in DTI parameters of the corpus callosum across groups

DTI	Comparison groups			N	P-value
FA	PE2max	vs	Wild type	30 : 18	1.000
		vs	Untreated	30 : 27	0.041*
		vs	AAV-null	30 : 39	0.230
	AAV-null	vs	Wild type	39 : 18	0.044*
		vs	Untreated	39 : 27	1.000
	Untreated	vs	Wild type	27 : 18	0.008**
AD	PE2max	vs	Wild type	24 : 18	1.000
		vs	Untreated	24 : 24	0.690
		vs	AAV-null	24 : 35	1.000
	AAV-null	vs	Wild type	35 : 18	0.005**
		vs	Untreated	35 : 24	1.000
	Untreated	vs	Wild type	24 : 18	<0.001***
RD	PE2max	vs	Wild type	30 : 14	1.000
		vs	Untreated	30 : 26	1.000
		vs	AAV-null	30 : 39	0.637
	AAV-null	vs	Wild type	39 : 14	1.000
		vs	Untreated	39 : 26	1.000
	Untreated	vs	Wild type	26 : 14	1.000
MD	PE2max	vs	Wild type	30 : 14	1.000
		vs	Untreated	30 : 27	1.000
		vs	AAV-null	30 : 39	1.000
	AAV-null	vs	Wild type	39 : 14	1.000
		vs	Untreated	39 : 27	1.000
	Untreated	vs	Wild type	27 : 14	1.000

Note: Values are expressed as means ± SEM. One-way ANOVA with Bonferroni's multiple comparison tests was conducted. Statistically significant differences are shown as $*P < 0.05$, $**P < 0.01$, and $***P < 0.001$.

3.9. Phenotype recovery was observed in the PE2max-treated group

In Twi mice, clinical symptoms typically begin to appear around P21, and most animals succumb to the disease before day 40. Early symptoms, such as head tremors, muscle rigidity, and weight loss, are associated with extensive demyelination and axonal degeneration in the nervous system. Affected mice exhibit markedly reduced activity compared with healthy controls, with progressive hindlimb weakness being one of the most prominent clinical features. In the terminal stages, voluntary movement is severely impaired. As body weight reflects overall physiological condition, it serves as a useful indirect biomarker for assessing therapeutic efficacy. To evaluate the effect of PE2max, body weight was monitored weekly from postnatal weeks 3 to 5. PE2max-treated mice exhibited a gradual increase in body weight, with a statistically significant elevation observed at week 5 (Figure 22 and Tables 21 and 22). Two-way ANOVA revealed significant main effects between groups as well as a significant group × time interaction, indicating that the therapeutic effects of PE2max accumulate over time rather than being transient. In addition, brain weight measured at the time of sacrifice on day 38 was markedly higher in the PE2max group compared with controls.

Collectively, the increases in body and brain weights provide physiological evidence that PE2max not only supports general systemic function but also positively contributes to structural development in the CNS of the Twi model.

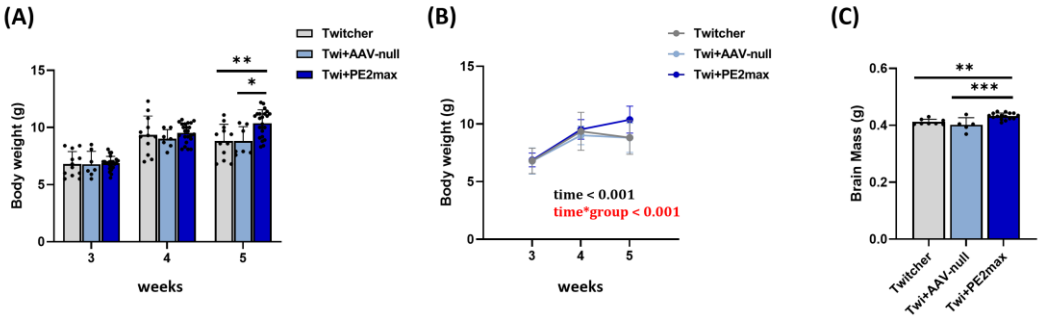

Figure 22. Evaluation of body weight and brain mass in Twitcher mice.

(A, B) Body weight was measured at weeks 3, 4, and 5. (C) Brain mass was measured at the experimental endpoint. (A, C) Bar graphs were analyzed using one-way ANOVA. (B) Line graph shows mean changes over time analyzed by two-way ANOVA, with time and group as variables. n = 5–15 per group. Values are expressed as means with error bars representing the standard error of the mean. One-way ANOVA with Bonferroni's multiple comparison tests was conducted. Statistically significant differences are shown as $*P < 0.05$, $**P < 0.01$, and $***P < 0.001$.

Table 21. Heterogeneity of variance in body weight and brain mass

Test	Week	Untreated	AAV-null	PE2max	F-value	P-value
Body weight	3	6.80 ± 0.32	6.79 ± 0.43	6.87 ± 0.12	0.045	0.956
	4	9.36 ± 0.47	9.01 ± 0.31	9.53 ± 0.18	0.583	0.563
	5	8.82 ± 0.42	8.80 ± 0.48	10.37 ± 0.24	7.824	<0.001***
Brain mass		0.41 ± 0.00	0.40 ± 0.01	0.43 ± 0.00	11.573	<0.001***

Note: Values are expressed as means ± SEM. One-way ANOVA with Bonferroni's multiple comparison tests was conducted. Statistically significant differences are shown as $*P < 0.05$, $**P < 0.01$, and $***P < 0.001$.

Table 22. Statistical analysis of group-wise differences in body weight and brain mass.

Test	Comparison groups			N	P-value
Body weight	PE2max	vs	Untreated	23 : 12	0.004**
	PE2max	vs	AAV-null	23 : 7	0.020*
	AAV-null	vs	Untreated	7 : 12	1.000
Brain mass	PE2max	vs	Untreated	16 : 8	0.007**
	PE2max	vs	AAV-null	16 : 5	<0.001***
	AAV-null	vs	Untreated	5 : 8	0.701

Note: Values are expressed as means ± SEM. One-way ANOVA with Bonferroni's multiple comparison tests was conducted. Statistically significant differences are shown as $*P < 0.05$, $**P < 0.01$, and $***P < 0.001$.

3.10. Confirmation of improved neurobehavioral function by behavioral assessments following PE2max treatment

This study used Twi mouse model to explore disease progression and therapeutic effects. In this model, symptoms generally begin to manifest around P21 (week 3), with early clinical indicators including head tremors, decreased body weight, and significantly reduced activity levels. As the condition progresses, severe muscle weakness—particularly in the hindlimbs—becomes apparent, accompanied by complications such as irritability, stiffness, seizures, and eventually paralysis.

To evaluate disease progression and therapeutic efficacy, behavioral assessments were uniformly conducted at weeks 3, 4, and 5 across all experimental groups. A battery of standardized behavioral tests was used to evaluate motor coordination, neuromuscular strength, and general activity, each selected to capture meaningful changes in functional ability. Considerable improvements were observed in the rotarod test, which was conducted to measure motor coordination and balance at week 5, alongside a time × group interaction suggesting progressive functional recovery (Figure 23). Similarly, the wire hanging test, used to assess muscular strength and endurance, also showed marked improvement and significant interaction effects at week 5 (Figure 26). In the clasping test, which reflects abnormal limb posture associated with neurological dysfunction, the treated group exhibited significant recovery at weeks 4 and 5 (Figure 25). In the cylinder test, which evaluates forelimb usage, significant differences were detected at weeks 3 and 5, indicating early onset and sustained treatment effects (Figure 24). In the open field test, consistent increases in total distance traveled across all time points were observed, with both main and interaction effects reaching statistical significance (Figure 27). In addition to functional improvements, the PE2max treatment significantly extended the lifespan of Twi mice. The mean survival was notably prolonged in the PE2max group than in the untreated and AAV-null controls (Figure 28A), which was further supported by the Kaplan–Meier survival analysis demonstrating a rightward shift in survival probability (Figure 28B). The daily

survival data, presented in the tabular form, also highlight a significantly increased survival rate in PE2max-treated animals beyond day 42 (Figure 28C), indicating delayed mortality and potential therapeutic benefit at the organismal level.

These findings collectively suggest that PE2max treatment confers functional and survival benefits in the Twi mouse model, highlighting its therapeutic potential for addressing the neurological and systemic manifestations of KD.

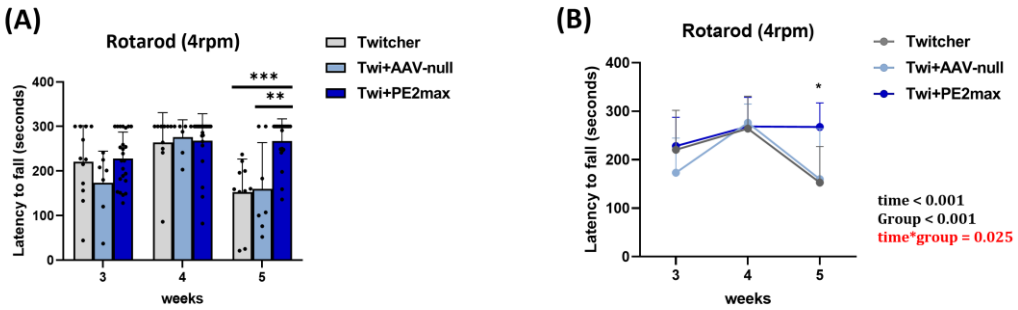

Figure 23. Assessment of rotarod performance at 4 rpm in the twitcher groups.

The latency time to fall from the rolling rod within 5 min was recorded. (A) Bar graphs were analyzed via one-way ANOVA, and (B) line graphs represent the mean changes in a quantitative variable based on two categorical factors, namely, time and disease conditions, as analyzed via two-way ANOVA. $n = 5–15$ per group. Values are expressed as means with error bars representing the standard error of the mean. One-way ANOVA with Bonferroni's multiple comparison tests was conducted. Statistically significant differences are shown as $*P < 0.05$, $**P < 0.01$, and $***P < 0.001$.

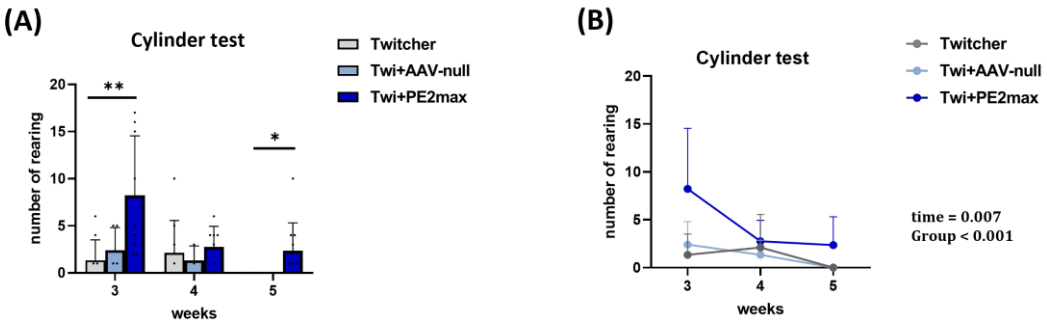

Figure 24. Assessment of rearing behavior in the cylinder test across the twitcher groups

(A) Bar graphs were analyzed via one-way ANOVA, and (B) line graphs represent the mean changes in a quantitative variable based on two categorical factors, namely, time and disease conditions, as analyzed via two-way ANOVA. $n = 5–15$ per group. Values are expressed as means with error bars representing the standard error of the mean. One-way ANOVA with Bonferroni's multiple comparison tests was conducted. Statistically significant differences are shown as $^{*}P < 0.05$, $^{**}P < 0.01$, and $^{***}P < 0.001$.

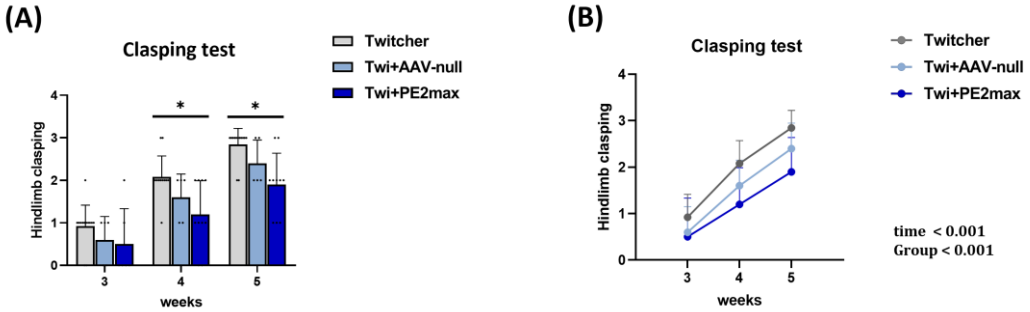

Figure 25. Assessment of hindlimb clasping behavior in the twitcher groups

The duration time of limb clasping under 10 s of tail suspension was monitored. (A) Bar graphs were analyzed via one-way ANOVA, and (B) line graphs represent the mean changes in a quantitative variable based on two categorical factors, namely, time and disease conditions, as analyzed via two-way ANOVA. $n = 5–15$ per group. Values are expressed as means with error bars representing the standard error of the mean. One-way ANOVA with Bonferroni's multiple comparison tests was conducted. Statistically significant differences are shown as $*P < 0.05$, $**P < 0.01$, and $***P < 0.001$.

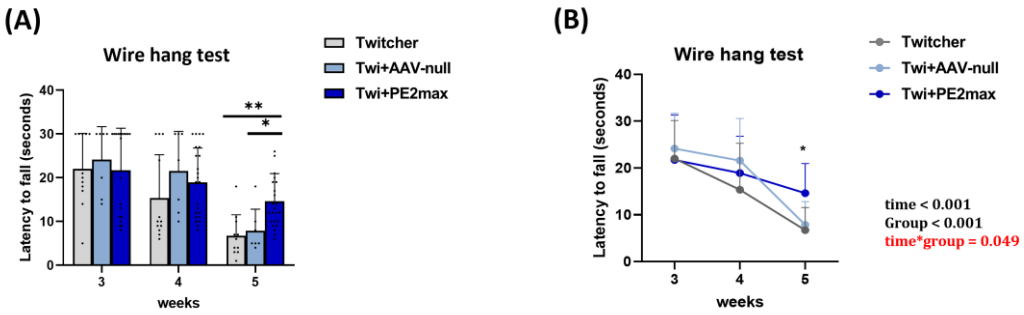

Figure 26. Assessment of grip strength and muscle endurance in the twitcher groups by wire hang test

(A) Bar graphs were analyzed via one-way ANOVA, and (B) line graphs represent the mean changes in a quantitative variable based on two categorical factors, namely, time and disease conditions, as analyzed via two-way ANOVA. $n = 5–15$ per group. Values are expressed as means with error bars representing the standard error of the mean. One-way ANOVA with Bonferroni's multiple comparison tests was conducted. Statistically significant differences are shown as $*P < 0.05$, $**P < 0.01$, and $***P < 0.001$.

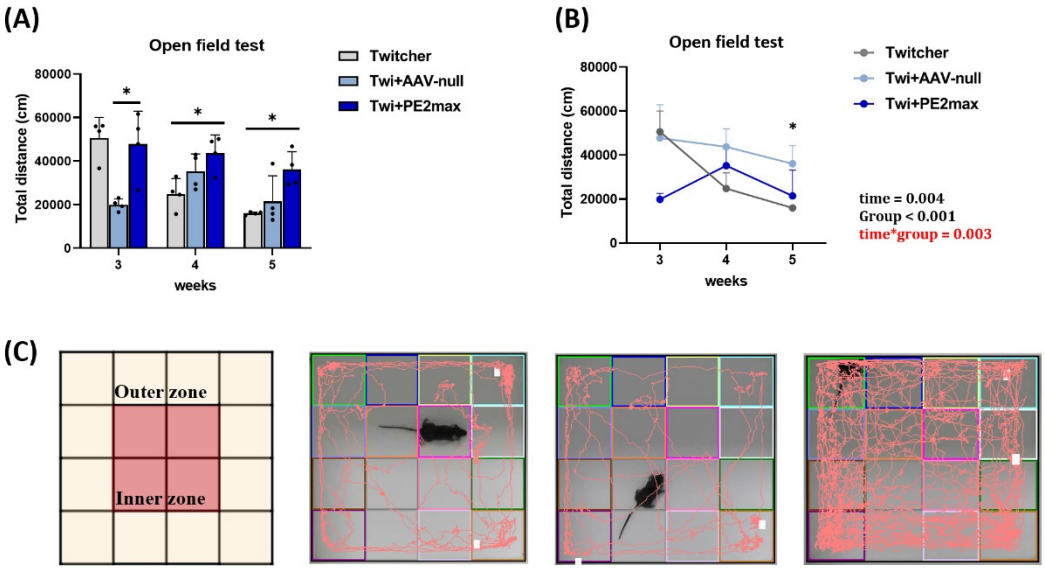

Figure 27. Assessment of locomotor activity in the twitcher groups using the open field test

(A) Bar graphs were analyzed via one-way ANOVA, and (B) line graphs represent the mean changes in a quantitative variable based on two categorical factors, namely, time and disease conditions, as analyzed via two-way ANOVA. (C) Representative movement traces and inner zone maps. $n = 5–15$ per group. Values are expressed as means with error bars representing the standard error of the mean. One-way ANOVA with Bonferroni's multiple comparison tests was conducted. Statistically significant differences are shown as $*P < 0.05$, $**P < 0.01$, and $***P < 0.001$.

Table 23. Heterogeneity of variance in behavioral assessments.

Test	Week	Untreated	AAV-null	PE2max	F-value	P-value
Rotarod Constant (4rpm)	3	220.33 ± 23.54	173.14 ± 27.03	228.00 ± 12.12	1.785	0.181
	4	264.10 ± 21.13	276.00 ± 14.64	268.57 ± 12.47	0.085	0.919
	5	152.80 ± 23.52	159.71 ± 39.30	267.52 ± 10.84	12.573	< 0.001***
Clasping	3	1.00 ± 0.17	0.60 ± 0.24	0.50 ± 0.34	1.332	0.290
	4	2.00 ± 0.17	1.60 ± 0.24	1.20 ± 0.25	3.619	0.045*
	5	2.78 ± 0.15	2.40 ± 0.24	1.90 ± 0.23	5.044	0.016*
Cylinder	3	1.33 ± 0.73	2.40 ± 1.08	8.22 ± 2.11	6.190	0.008**
	4	2.11 ± 1.15	1.33 ± 0.88	2.75 ± 0.77	0.300	0.745
	5	0.00 ± 0.00	0.00 ± 0.00	2.36 ± 0.89	4.374	0.025*
Wire hang	3	22.00 ± 2.35	26.29 ± 2.49	21.70 ± 2.15	0.758	0.476
	4	15.33 ± 2.87	21.57 ± 3.41	18.91 ± 1.64	1.253	0.297
	5	6.73 ± 1.45	7.86 ± 1.87	14.63 ± 1.29	8.647	<0.001***
Open field	3	50660.47 ± 4675.25	19924.07 ± 1365.91	47770.23 ± 7554.91	10.696	0.004**
	4	24843.16 ± 3546.47	35209.98 ± 4055.31	43753.19 ± 4100.30	5.869	0.023*
	5	16017.39 ± 343.01	21503.22 ± 5870.38	36105.03 ± 4092.38	6.301	0.019*

Note: Values are expressed as means ± SEM. One-way ANOVA with Bonferroni's multiple comparison tests was conducted. Statistically significant differences are shown as *$P < 0.05$, **$P < 0.01$, and ***$P < 0.001$.

Table 24. Statistical analysis of group-wise differences in behavioral assessments.

Test	Week	Comparison groups			N	P-value
Rotarod Constant (4rpm)	3	PE2max	vs	Untreated	24 : 12	1.000
		PE2max	vs	AAV-null	24 : 7	0.203
		AAV-null	vs	Untreated	7 : 12	0.457
	4	PE2max	vs	Untreated	23 : 10	1.000
		PE2max	vs	AAV-null	23 : 7	1.000
		AAV-null	vs	Untreated	7 : 10	1.000
	5	PE2max	vs	Untreated	21 : 10	<0.001***
		PE2max	vs	AAV-null	21 : 7	0.003**
		AAV-null	vs	Untreated	7 : 10	1.000
Clasping	3	PE2max	vs	Untreated	6 : 9	0.447
		PE2max	vs	AAV-null	6 : 5	1.000
		AAV-null	vs	Untreated	5 : 9	0.807
	4	PE2max	vs	Untreated	10 : 9	0.041*
		PE2max	vs	AAV-null	10 : 5	0.816
		AAV-null	vs	Untreated	5 : 9	0.841
	5	PE2max	vs	Untreated	10 : 9	0.014*
		PE2max	vs	AAV-null	10 : 5	0.436
		AAV-null	vs	Untreated	5 : 9	0.824
Cylinder	3	PE2max	vs	Untreated	9 : 9	0.010*
		PE2max	vs	AAV-null	9 : 5	0.080
		AAV-null	vs	Untreated	5 : 9	1.000
	4	PE2max	vs	Untreated	8 : 9	1.000
		PE2max	vs	AAV-null	8 : 3	1.000
		AAV-null	vs	Untreated	3 : 9	1.000
	5	PE2max	vs	Untreated	11 : 9	0.044*
		PE2max	vs	AAV-null	11 : 5	0.114
		AAV-null	vs	Untreated	5 : 9	1.000

Wire hang	3	PE2max	vs	Untreated	20 : 12	1.000
		PE2max	vs	AAV-null	20 : 7	0.718
		AAV-null	vs	Untreated	7 : 12	0.927
	4	PE2max	vs	Untreated	23 : 12	0.763
		PE2max	vs	AAV-null	23 : 7	1.000
		AAV-null	vs	Untreated	7 : 12	0.417
	5	PE2max	vs	Untreated	24 : 11	0.002**
		PE2max	vs	AAV-null	24 : 7	0.029*
		AAV-null	vs	Untreated	7 : 11	1.000
Open field	3	PE2max	vs	Untreated	4 : 4	1.000
		PE2max	vs	AAV-null	4 :4	0.013*
		AAV-null	vs	Untreated	4 : 4	0.007**
	4	PE2max	vs	Untreated	4 :4	0.023*
		PE2max	vs	AAV-null	4 : 4	0.470
		AAV-null	vs	Untreated	4 :4	0.280
	5	PE2max	vs	Untreated	4 : 4	0.022*
		PE2max	vs	AAV-null	4 :4	0.102
		AAV-null	vs	Untreated	4 :4	1.000

Note: Values are expressed as means ± SEM. One-way ANOVA with Bonferroni's multiple comparison tests was conducted. Statistically significant differences are shown as $*P < 0.05$, $**P < 0.01$, and $***P < 0.001$.

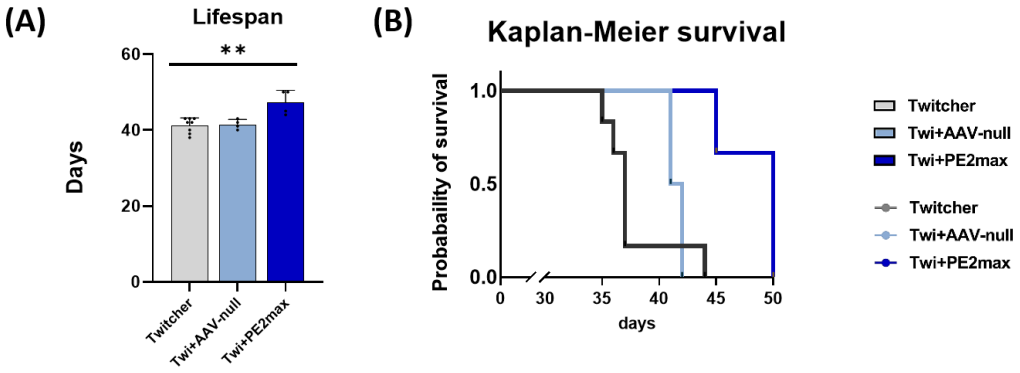

(C)

	Untreated	control	PE2max	Chi square	*P*-value
36 days	100%	100%	100%	-	-
37 days	100%	100%	100%	-	-
38 days	87.5	100%	100%	1.000	0.587
39 days	75	100%	100%	2.286	0.319
40 days	62.5%	75%	100%	2.000	0.368
41 days	62.5%	50%	100%	0.618	0.270
42 days	37.5%	25%	100%	5.500	0.064
43 days	0%	0%	100%	16.000	0.000
44 days	0%	0%	75%	11.077	0.004
45 days	0%	0%	50%	6.857	0.032
46 days	0%	0%	50%	6.857	0.032
47 days	0%	0%	50%	6.857	0.032
48 days	0%	0%	50%	6.857	0.032
49 days	0%	0%	50%	6.857	0.032

Figure 28. The PE-treated groups exhibited increased lifespan compared with the control groups

(A) The estimated mean lifespan was calculated, and statistical analysis was conducted via one-way ANOVA with Bonferroni correction. (B) Cumulative survival curves were plotted using the Kaplan–Meier method, and significance was evaluated using the log-rank test. Interval survival analysis from P36 to P49 was also evaluated using the log-rank test. (C) A summary table shows the survival rate for each group, with proportions visualized in gradient blue based on survival percentages and corresponding chi-squared values. Significant differences are shown as $*P < 0.05$, $**P < 0.01$, and $***P < 0.001$.

3.11. No signs of tumor formation or dysplasia were observed in the brain or organs after PE therapy

To evaluate biosafety, histological analyses were conducted on major organs—including the brain, liver, kidney, spleen, and lung—via hematoxylin and eosin staining. No evidence of abnormal cell proliferation, neoplastic lesions, or architectural distortion indicating dysplasia was detected across all examined tissues from PE2max-treated mice (Figures 29 and 30). These findings were consistent with those of the WT, Twi, and empty AAV control groups, indicating that systemic AAV-PE2max delivery does not induce histopathological toxicity or tumor-related complications.

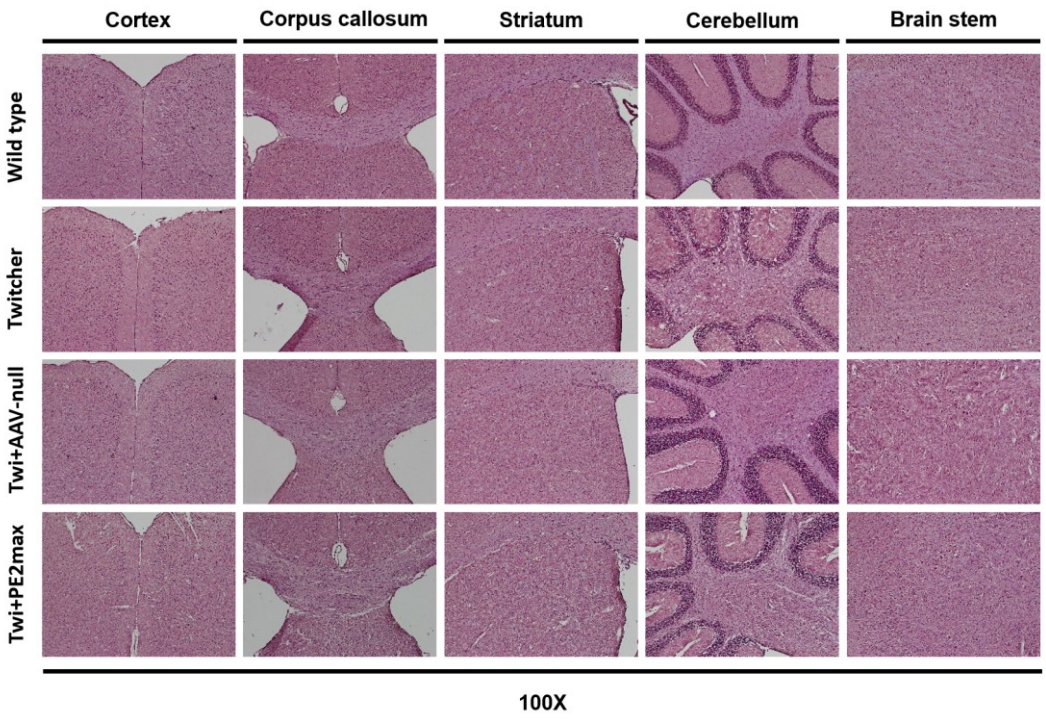

Figure 29. Hematoxylin and eosin staining of five brain regions

Representative hematoxylin and eosin (H&E)-stained brain sections. The regions shown are the cortex, corpus callosum, striatum, cerebellum, and brainstem. Images were captured at a 100× magnification.

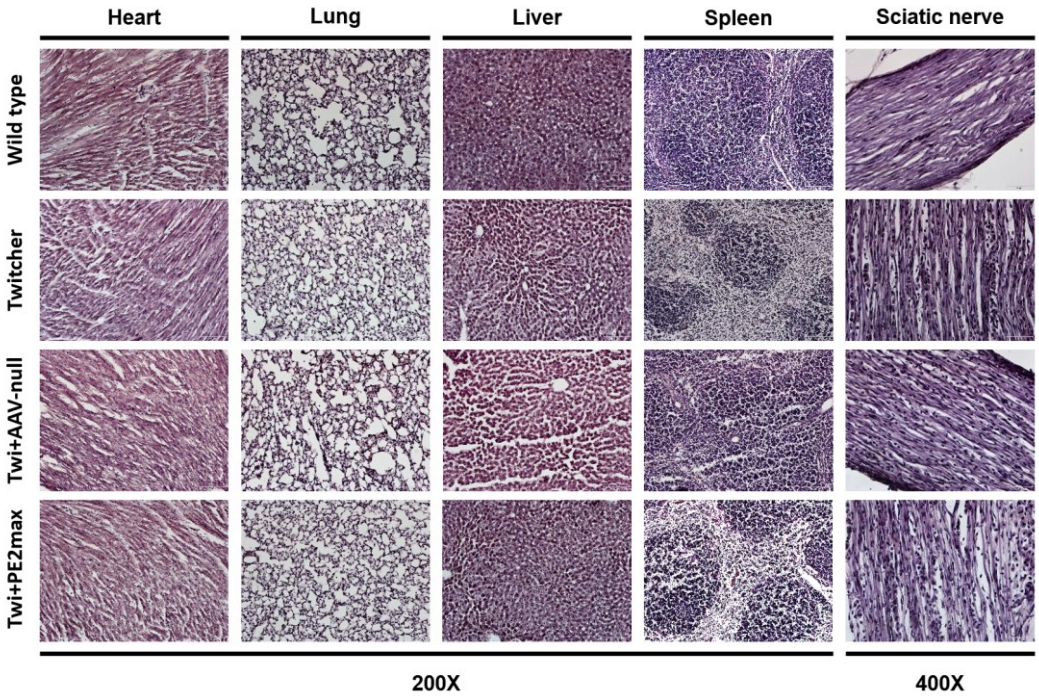

Figure 30. Hematoxylin and eosin staining of five peripheral organs

Representative hematoxylin and eosin (H&E)-stained sections of peripheral organs. The organs shown are the heart, lung, liver, spleen (200×), and sciatic nerve (400×).

3.12. No behavioral abnormalities observed in wild-type mice: safety confirmation of PE2max administered at P1

To evaluate the safety of systemic AAV-PE2max administration in healthy animals, WT mice were intravenously injected at P1 and subsequently assessed for any behavioral alterations. A comprehensive battery of motor and activity-based tests—including body weight monitoring, rotarod performance at multiple speeds (4, 12, and 4–40 rpm), and wire hanging test—was conducted at weeks 3, 4, and 5 after the injection. No statistically significant differences were observed between PE2max-injected WT mice and their vehicle- or AAV-null-treated counterparts across all assays. Body weight gain followed a normal developmental trajectory (Figure 31A), and the rotarod and wire hanging test performances remained within the physiological range of untreated WT animals (Figures 31B–E). These results suggest that neonatal systemic delivery of PE2max does not adversely affect gross motor coordination, neuromuscular strength, balance, or physical growth in healthy animals.

The data collectively confirm the behavioral safety of PE2max when administered at the neonatal stage, demonstrating its suitability as a nontoxic gene editing method for *in vivo* applications.

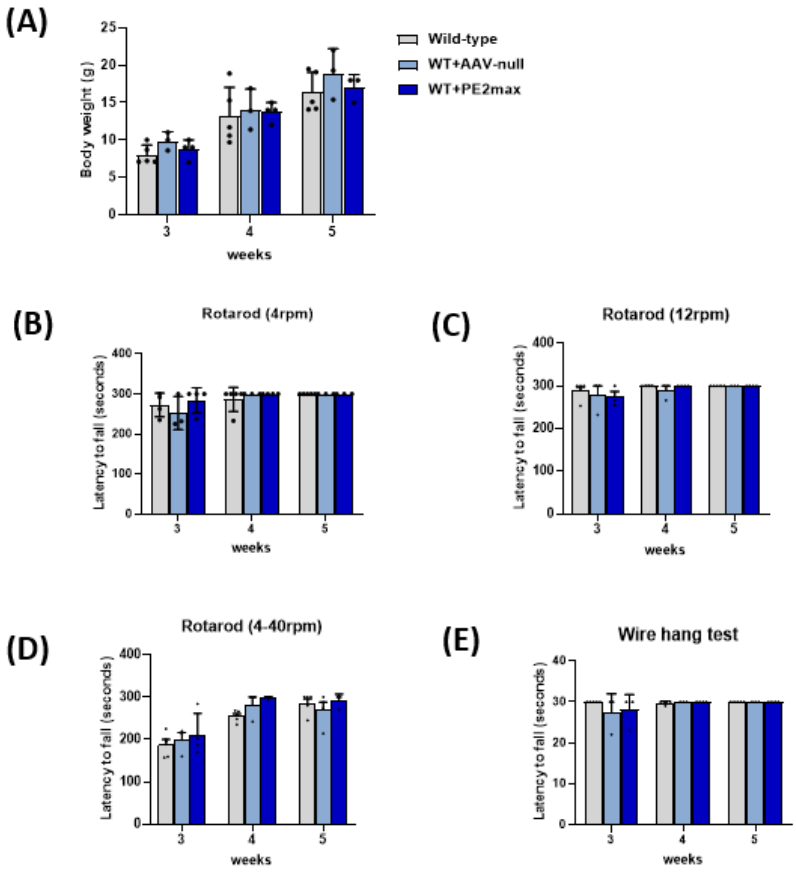

Figure 31. Behavioral assessment of wild-type mice after P1 intravenous injection.
(A) Body weight of mice from 3 to 5 weeks of age. (B–D) Motor coordination and balance evaluated using the rotarod test at constant (4 and 12 rpm) and accelerating (4–40 rpm) speeds. (E) Muscle strength measured using the wire hanging test. $n = 5–15$ per group. Values are expressed as means with error bars representing the standard error of the mean (SEM). All statistical comparisons were performed using Bonferroni-adjusted *post hoc* tests; significant differences are shown as $*P < 0.05$, $**P < 0.01$, and $***P < 0.001$.

Table 25. Heterogeneity of variance in behavioral assessments.

Test	Week	Untreated	AAV-null	PE2max	F-value	P-value
Body weight	3	8.02 ± 0.58	9.87 ± 0.70	8.75 ± 0.63	1.999	0.191
	4	13.24 ± 1.71	14.07 ± 1.59	13.75 ± 0.63	0.080	0.924
	5	16.40 ± 1.20	18.90 ± 1.92	17.00 ± 1.00	0.844	0.465
Rotarod Constant (4rpm)	3	238.60 ± 35.79	252.33 ± 23.92	284.50 ± 15.50	0.674	0.534
	4	286.60 ± 13.40	300.00 ± 0.00	300.00 ± 0.00	0.656	0.542
	5	300.00 ± 0.00	300.00 ± 0.00	300.00 ± 0.00	-	-
Rotarod Constant (12rpm)	3	288.50 ± 9.21	277.33 ± 22.67	250.42 ± 25.06	1.205	0.344
	4	299.60 ± 0.40	288.67 ± 11.33	300.00 ± 0.00	1.617	0.251
	5	300.00 ± 0.00	300.00 ± 0.00	300.00 ± 0.00	-	-
Rotarod accelerated (4-40rpm)	3	187.20 ± 12.96	197.67 ± 18.94	210.75 ± 25.28	0.421	0.669
	4	254.80 ± 6.09	280.67 ± 19.33	269.00 ± 19.09	0.800	0.479
	5	285.00 ± 10.72	298.00 ± 2.00	290.00 ± 10.00	0.434	0.663
Wire hang	3	30.00 ± 0.00	27.33 ± 2.67	28.25 ± 1.75	0.841	0.463
	4	29.80 ± 0.20	30.00 ± 0.00	30.00 ± 0.00	0.656	0.542
	5	30.00 ± 0.00	30.00 ± 0.00	30.00 ± 0.00	-	-

Note: Values are expressed as means ± SEM. One-way ANOVA with Bonferroni's multiple comparison tests was conducted. Statistically significant differences are shown as $*P < 0.05$, $**P < 0.01$, and $***P < 0.001$.

Table 26. Statistical analysis of group-wise differences in behavioral assessments.

Test	Week	Comparison groups			N	P-value
Body weight	3	PE2max	vs	Untreated	4 : 5	1.000
		PE2max	vs	AAV-null	4 : 3	0.833
		AAV-null	vs	Untreated	3 : 5	0.230
	4	PE2max	vs	Untreated	4 : 5	1.000
		PE2max	vs	AAV-null	4 : 3	1.000
		AAV-null	vs	Untreated	3 : 5	1.000
	5	PE2max	vs	Untreated	4 : 5	1.000
		PE2max	vs	AAV-null	4 : 3	1.000
		AAV-null	vs	Untreated	3 : 5	0.704
Rotarod Constant (4rpm)	3	PE2max	vs	Untreated	4 : 5	0.841
		PE2max	vs	AAV-null	4 : 3	1.000
		AAV-null	vs	Untreated	3 : 5	1.000
	4	PE2max	vs	Untreated	4 : 5	1.000
		PE2max	vs	AAV-null	4 : 3	1.000
		AAV-null	vs	Untreated	3 : 5	1.000
	5	PE2max	vs	Untreated	4 : 5	-
		PE2max	vs	AAV-null	4 : 3	-
		AAV-null	vs	Untreated	3 : 5	-
Rotarod Constant (12rpm)	3	PE2max	vs	Untreated	4 : 5	0.478
		PE2max	vs	AAV-null	4 : 3	1.000
		AAV-null	vs	Untreated	3 : 5	1.000
	4	PE2max	vs	Untreated	4 : 5	1.000
		PE2max	vs	AAV-null	4 : 3	0.432
		AAV-null	vs	Untreated	3 : 5	0.432
	5	PE2max	vs	Untreated	4 : 5	-
		PE2max	vs	AAV-null	4 : 3	-
		AAV-null	vs	Untreated	3 : 5	-

Rotarod accelerated (4-40rpm)	3	PE2max	vs	Untreated	4 : 5	1.000
		PE2max	vs	AAV-null	4 : 3	1.000
		AAV-null	vs	Untreated	3 : 5	1.000
	4	PE2max	vs	Untreated	4 : 5	1.000
		PE2max	vs	AAV-null	4 : 3	1.000
		AAV-null	vs	Untreated	3 : 5	0.740
	5	PE2max	vs	Untreated	4 : 5	1.000
		PE2max	vs	AAV-null	4 : 3	1.000
		AAV-null	vs	Untreated	3 : 5	1.000
Wire hang	3	PE2max	vs	Untreated	4 : 5	1.000
		PE2max	vs	AAV-null	4 : 3	1.000
		AAV-null	vs	Untreated	3 : 5	0.750
	4	PE2max	vs	Untreated	4 : 5	1.000
		PE2max	vs	AAV-null	4 : 3	1.000
		AAV-null	vs	Untreated	3 : 5	1.000
	5	PE2max	vs	Untreated	4 : 5	-
		PE2max	vs	AAV-null	4 : 3	-
		AAV-null	vs	Untreated	3 : 5	-

Note: Values are expressed as means ± SEM. One-way ANOVA with Bonferroni's multiple comparison tests was conducted. Statistically significant differences are shown as $*P < 0.05$, $**P < 0.01$, and $***P < 0.001$.

4. DISCUSSION

This study reports the first successful use of single-nucleotide PE with the PE2max system in a KD mouse model, demonstrating both molecular correction and therapeutic efficacy. Precise correction of the disease-causing point mutation in the *Galc* gene of Twi mice enabled the restoration of GALC expression and enzymatic activity, leading to considerable improvements in biochemical, histological, and behavioral outcomes.

PE enabled precise A-to-G substitution without detectable off-target effects, as confirmed by deep sequencing of genomic DNA and cDNA. Notably, the editing efficiency was the highest in the CNS regions, such as the FC, BS, and SC, which also exhibited the most pronounced therapeutic responses. This regional specificity likely reflects differences in AAV vector tropism and tissue accessibility. In particular, AAV-PHP.eB has shown significantly higher efficiency in crossing the BBB than its parental serotype AAV9, enabling widespread transduction of CNS tissues[33,37,38]. These characteristics are supported by the distinct biodistribution patterns of vector genomes, quantified by qPCR, which closely match the distribution of fluorescent reporter signals observed in previous studies. These studies demonstrated robust transgene expression in the brain and spinal cord following systemic AAV-PHP.eB administration. Restoration of GALC enzymatic function was accompanied by a considerable reduction in the levels of psychosine, a key neurotoxic lipid that accumulates in GALC-deficient tissues[16,39]. As psychosine plays a pivotal role in KD pathogenesis—disrupting lipid rafts, impairing cell signaling, and inducing demyelination—its reduction serves as evidence of functional correction of the underlying metabolic defect[16,36]. This effect was further supported by increased MBP expression, as revealed by IF staining, indicating enhanced remyelination or preservation of myelin sheaths. Results of histological analyses reinforced these molecular findings. LFB staining demonstrated increased myelin intensity and structural restoration of myelin sheaths, particularly in the CC. Moreover, the number of PAS-positive globoid cells—a pathological hallmark of neuroinflammation[40,41]— was markedly decreased in treated mice. These

results indicate that PE not only repairs the genetic defect but also alleviates downstream inflammatory and degenerative processes.

Nevertheless, several limitations remain. The dual-AAV delivery system, using the AAV-PHP.eB and AAV-MaCPNS1 vectors, enabled widespread distribution of PE2max components in the CNS and PNS[28,42]. However, prime editing efficiency in the sciatic nerve was markedly lower than in CNS regions. This observation highlights the need for further optimization of vector design and delivery strategies to enhance editing in peripheral nerves[43,44]. Previous studies have demonstrated that AAV-MaCPNS1 achieves robust transduction of sensory ganglia, particularly dorsal root ganglia (DRG), following systemic administration[28]. In contrast, both our findings and prior reports indicate that MaCPNS1 exhibits limited transduction and gene editing efficiency in the sciatic nerve, likely due to differences in cellular composition, extracellular matrix barriers, and vector accessibility between DRG and peripheral nerve tissues[44,45]. Additionally, it has been shown that certain AAV serotypes, such as AAV-rh10, can more effectively target Schwann cells in the sciatic nerve when delivered intrathecally[46-48], suggesting that alternative capsids or administration routes may be necessary for efficient gene editing in specific PNS compartments. Furthermore, factors such as promoter selection and timing of delivery are critical determinants of transduction efficiency and cell-type specificity in the PNS[32,49]. To address this problem, we are currently conducting additional experiments using single-dose administration to more accurately evaluate and enhance editing efficiency in the PNS. Notably, no significant adverse effects were observed in either WT or mutant mice, and the indel rates remained at background levels. This confirms the high precision and safety of PE2max, which prevents DSBs and minimizes genotoxicity.

As KD is a monogenic disorder, PE provides a particularly suitable therapeutic approach by directly correcting the causative mutation *in situ*. In addition to vector optimization, further improvements in pegRNA design, vector tropism, and delivery timing may enhance the overall editing efficacy. Moreover, long-term studies are warranted to evaluate the durability of gene correction and the potential for delayed adverse effects. The combination

of PE with other therapeutic strategies, such as HSCT, may offer synergistic benefits by addressing central and peripheral pathological mechanisms.

In conclusion, our findings indicate the feasibility and therapeutic promise of PE for KD. This study lays the groundwork for future clinical applications of precise genome-editing technologies in lysosomal storage disorders and other monogenic neurodevelopmental conditions.

5. CONCLUSION

In conclusion, this study provides the first *in vivo* evidence that single-nucleotide PE using the PE2max system can effectively correct the causative mutation of KD in a mouse model, which results in molecular restoration and meaningful therapeutic benefit. Our results indicate precise A-to-G base editing with minimal off-target effects, robust GALC enzymatic recovery, and marked improvements in myelination and behavioral phenotypes, particularly in CNS regions. Although the editing efficiency in the PNS remains suboptimal, likely due to vector tropism limitations, our ongoing efforts to optimize delivery strategies and vector components hold promise for peripheral correction enhancement. Notably, the absence of detectable toxicity and indel formation highlights the safety of PE2max-mediated PE. Collectively, these findings establish a foundational proof-of-concept for the use of PE as a viable and precise therapeutic approach for monogenic neurodegenerative diseases, such as KD, and pave the way for its further translational development.

REFERANCE

1 Wenger, D. A., Rafi, M. A., Luzi, P., Datto, J. & Costantino-Ceccarini, E. Krabbe disease: genetic aspects and progress toward therapy. *Mol Genet Metab* **70**, 1-9 (2000). https://doi.org/10.1006/mgme.2000.2990

2 Vantaggiato, L. *et al.* Neurodegenerative Disorder Risk in Krabbe Disease Carriers. *Int J Mol Sci* **23** (2022). https://doi.org/10.3390/ijms232113537

3 Tonazzini, I. *et al.* Visual System Impairment in a Mouse Model of Krabbe Disease: The Twitcher Mouse. *Biomolecules* **11** (2020). https://doi.org/10.3390/biom11010007

4 Won, J. S., Singh, A. K. & Singh, I. Biochemical, cell biological, pathological, and therapeutic aspects of Krabbe's disease. *J Neurosci Res* **94**, 990-1006 (2016). https://doi.org/10.1002/jnr.23873

5 Brites, P. & Sousa, M. M. Neurons contribute to pathology in a mouse model of Krabbe disease in a cell-autonomous manner. *PLoS Biol* **20**, e3001706 (2022). https://doi.org/10.1371/journal.pbio.3001706

6 Potter, G. B. *et al.* Missense mutation in mouse GALC mimics human gene defect and offers new insights into Krabbe disease. *Hum Mol Genet* **22**, 3397-3414 (2013). https://doi.org/10.1093/hmg/ddt190

7 Feltri, M. L. *et al.* Mechanisms of demyelination and neurodegeneration in globoid cell leukodystrophy. *Glia* **69**, 2309-2331 (2021). https://doi.org/10.1002/glia.24008

8 Haq, E., Giri, S., Singh, I. & Singh, A. K. Molecular mechanism of psychosine-induced cell death in human oligodendrocyte cell line. *J Neurochem* **86**, 1428-1440 (2003). https://doi.org/10.1046/j.1471-4159.2003.01941.x

9 Won, J. S., Kim, J., Paintlia, M. K., Singh, I. & Singh, A. K. Role of endogenous psychosine accumulation in oligodendrocyte differentiation and survival: implication for Krabbe disease. *Brain Res* **1508**, 44-52 (2013). https://doi.org/10.1016/j.brainres.2013.02.024

10 Jatana, M., Giri, S. & Singh, A. K. Apoptotic positive cells in Krabbe brain and induction of apoptosis in rat C6 glial cells by psychosine. *Neurosci Lett* **330**, 183-187 (2002). https://doi.org/10.1016/s0304-3940(02)00655-9

11 Castelvetri, L. C. *et al.* Axonopathy is a compounding factor in the pathogenesis of Krabbe disease. *Acta Neuropathol* **122**, 35-48 (2011). https://doi.org/10.1007/s00401-011-0814-2

12 Escolar, M. L. *et al.* Transplantation of umbilical-cord blood in babies with infantile Krabbe's disease. *N Engl J Med* **352**, 2069-2081 (2005). https://doi.org/10.1056/NEJMoa042604

13 Kemper, A. R. *et al.* Weighing the evidence for newborn screening for early-infantile Krabbe disease. *Genet Med* **12**, 539-543 (2010). https://doi.org/10.1097/GIM.0b013e3181e85721

14 Zawadzka, M. & Franklin, R. J. Myelin regeneration in demyelinating disorders: new developments in biology and clinical pathology. *Curr Opin Neurol* **20**, 294-298 (2007). https://doi.org/10.1097/WCO.0b013e32813aee7f

15 Weinstock, N. I. *et al.* Brainstem development requires galactosylceramidase and is critical for pathogenesis in a model of Krabbe disease. *Nat Commun* **11** (2020). https://doi.org/ARTN 5356, 10.1038/s41467-020-19179-w

16 Rafi, M. A., Rao, H. Z., Luzi, P. & Wenger, D. A. Long-term Improvements in Lifespan and Pathology in CNS and PNS After BMT Plus One Intravenous Injection of AAVrh10-GALC in Twitcher Mice. *Mol Ther* **23**, 1681-1690 (2015). https://doi.org/10.1038/mt.2015.145

17 Biffi, A. *et al.* Lentiviral hematopoietic stem cell gene therapy benefits metachromatic leukodystrophy. *Science* **341**, 1233158 (2013). https://doi.org/10.1126/science.1233158

18 Anzalone, A. V. *et al.* Search-and-replace genome editing without double-strand breaks or donor DNA. *Nature* **576**, 149-157 (2019). https://doi.org/10.1038/s41586-019-1711-4

19 Anzalone, A. V., Koblan, L. W. & Liu, D. R. Genome editing with CRISPR-Cas nucleases, base editors, transposases and prime editors. *Nat Biotechnol* **38**, 824-844 (2020). https://doi.org/10.1038/s41587-020-0561-9

20 Lin, Q. *et al.* Prime genome editing in rice and wheat. *Nat Biotechnol* **38**, 582-585 (2020). https://doi.org/10.1038/s41587-020-0455-x

21 Weidmann, C. A., Mustoe, A. M., Jariwala, P. B., Calabrese, J. M. & Weeks, K. M. Analysis of RNA-protein networks with RNP-MaP defines functional hubs on RNA. *Nat Biotechnol* **39**, 347-356 (2021). https://doi.org/10.1038/s41587-020-0709-7

22 Chen, P. J. & Liu, D. R. Prime editing for precise and highly versatile genome manipulation. *Nat Rev Genet* **24**, 161-177 (2023). https://doi.org/10.1038/s41576-022-00541-1

23 Hillary, V. E. & Ceasar, S. A. Prime editing in plants and mammalian cells: Mechanism, achievements, limitations, and future prospects. *Bioessays* **44**, e2200032 (2022). https://doi.org/10.1002/bies.202200032

24 Schene, I. F. *et al.* Prime editing for functional repair in patient-derived disease models. *Nat Commun* **11**, 5352 (2020). https://doi.org/10.1038/s41467-020-19136-7

25 Qu, Y., Liu, Y., Noor, A. F., Tran, J. & Li, R. Characteristics and advantages of adeno-associated virus vector-mediated gene therapy for neurodegenerative diseases. *Neural Regen Res* **14**, 931-938 (2019). https://doi.org/10.4103/1673-5374.250570

26 Zwi-Dantsis, L., Mohamed, S., Massaro, G. & Moeendarbary, E. Adeno-Associated Virus Vectors: Principles, Practices, and Prospects in Gene Therapy. *Viruses* **17** (2025). https://doi.org/10.3390/v17020239

27 Hudry, E. & Vandenberghe, L. H. Therapeutic AAV Gene Transfer to the Nervous System: A Clinical Reality. *Neuron* **102**, 263 (2019). https://doi.org/10.1016/j.neuron.2019.03.020

28 Chan, K. Y. *et al.* Engineered AAVs for efficient noninvasive gene delivery to the central and peripheral nervous systems. *Nat Neurosci* **20**, 1172-1179 (2017). https://doi.org/10.1038/nn.4593

29 Wu, Z., Yang, H. & Colosi, P. Effect of genome size on AAV vector packaging. *Mol Ther* **18**, 80-86 (2010). https://doi.org/10.1038/mt.2009.255

30 Hirsch, M. L., Wolf, S. J. & Samulski, R. J. Delivering Transgenic DNA Exceeding the Carrying Capacity of AAV Vectors. *Methods Mol Biol* **1382**, 21-39 (2016).

https://doi.org/10.1007/978-1-4939-3271-9_2

31 Puhl, D. L., D'Amato, A. R. & Gilbert, R. J. Challenges of gene delivery to the central nervous system and the growing use of biomaterial vectors. *Brain Res Bull* **150**, 216-230 (2019). https://doi.org/10.1016/j.brainresbull.2019.05.024

32 O'Carroll, S. J., Cook, W. H. & Young, D. AAV Targeting of Glial Cell Types in the Central and Peripheral Nervous System and Relevance to Human Gene Therapy. *Front Mol Neurosci* **13**, 618020 (2020). https://doi.org/10.3389/fnmol.2020.618020

33 Chatterjee, D. *et al.* Enhanced CNS transduction from AAV.PHP.eB infusion into the cisterna magna of older adult rats compared to AAV9. *Gene Ther* **29**, 390-397 (2022). https://doi.org/10.1038/s41434-021-00244-y

34 De Gasperi, R. *et al.* Transgenic rescue of Krabbe disease in the twitcher mouse. *Gene Ther* **11**, 1188-1194 (2004). https://doi.org/10.1038/sj.gt.3302282

35 Del Grosso, A. *et al.* Chronic lithium administration in a mouse model for Krabbe disease. *JIMD Rep* **63**, 50-65 (2022). https://doi.org/10.1002/jmd2.12258

36 White, A. B. *et al.* Psychosine accumulates in membrane microdomains in the brain of krabbe patients, disrupting the raft architecture. *J Neurosci* **29**, 6068-6077 (2009). https://doi.org/10.1523/JNEUROSCI.5597-08.2009

37 Goertsen, D. *et al.* AAV capsid variants with brain-wide transgene expression and decreased liver targeting after intravenous delivery in mouse and marmoset. *Nat Neurosci* **25**, 106-115 (2022). https://doi.org/10.1038/s41593-021-00969-4

38 Mathiesen, S. N., Lock, J. L., Schoderboeck, L., Abraham, W. C. & Hughes, S. M. CNS Transduction Benefits of AAV-PHP.eB over AAV9 Are Dependent on Administration Route and Mouse Strain. *Mol Ther Methods Clin Dev* **19**, 447-458 (2020). https://doi.org/10.1016/j.omtm.2020.10.011

39 Ricca, A. *et al.* Combined gene/cell therapies provide long-term and pervasive rescue of multiple pathological symptoms in a murine model of globoid cell leukodystrophy. *Hum Mol Genet* **24**, 3372-3389 (2015). https://doi.org/10.1093/hmg/ddv086

40 Hawkins-Salsbury, J. A. *et al.* Mechanism-based combination treatment dramatically increases therapeutic efficacy in murine globoid cell leukodystrophy. *J Neurosci* **35**, 6495-6505 (2015). https://doi.org/10.1523/JNEUROSCI.4199-14.2015

41 Kondo, Y., Adams, J. M., Vanier, M. T. & Duncan, I. D. Macrophages counteract demyelination in a mouse model of globoid cell leukodystrophy. *J Neurosci* **31**, 3610-3624 (2011). https://doi.org/10.1523/JNEUROSCI.6344-10.2011

42 Morabito, G. *et al.* AAV-PHP.B-Mediated Global-Scale Expression in the Mouse Nervous System Enables GBA1 Gene Therapy for Wide Protection from Synucleinopathy. *Mol Ther* **25**, 2727-2742 (2017). https://doi.org/10.1016/j.ymthe.2017.08.004

43 Mason, M. R. *et al.* Comparison of AAV serotypes for gene delivery to dorsal root ganglion neurons. *Mol Ther* **18**, 715-724 (2010). https://doi.org/10.1038/mt.2010.19

44 Schuster, D. J. *et al.* Biodistribution of adeno-associated virus serotype 9 (AAV9) vector after intrathecal and intravenous delivery in mouse. *Front Neuroanat* **8**, 42 (2014). https://doi.org/10.3389/fnana.2014.00042

45 Hordeaux, J. *et al.* Adeno-Associated Virus-Induced Dorsal Root Ganglion Pathology. *Hum Gene Ther* **31**, 808-818 (2020). https://doi.org/10.1089/hum.2020.167

46 Hordeaux, J. *et al.* The Neurotropic Properties of AAV-PHP.B Are Limited to C57BL/6J Mice. *Mol Ther* **26**, 664-668 (2018). https://doi.org/10.1016/j.ymthe.2018.01.018

47 Christou, M. *et al.* A dose escalation and safety study of AAVrh10-mediated Schwann cell-targeted gene therapy for CMT1X. *Neurotherapeutics* **22**, e00568 (2025). https://doi.org/10.1016/j.neurot.2025.e00568

48 Kagiava, A. *et al.* Efficacy of AAV serotypes to target Schwann cells after intrathecal and intravenous delivery. *Sci Rep* **11**, 23358 (2021). https://doi.org/10.1038/s41598-021-02694-1

49 Yang, O. J. *et al.* Evaluating the transduction efficiency of systemically delivered AAV vectors in the rat nervous system. *Front Neurosci* **17**, 1001007 (2023). https://doi.org/10.3389/fnins.2023.1001007

ABSTRACT (IN KOREAN)

PE2max 기반 프라임 편집을 통한 크라베병 모델에서의 갈락토실세라마이드분해효소 기능 및 신경행동 이상 복구

Krabbe병은 갈락토실세라마디아제(GALC) 유전자의 돌연변이로 인해 발생하는 생명을 위협하는 리소좀 축적 질환으로, 사이코신의 축적, 탈수초, 중추신경계 및 말초신경계의 신경퇴행을 초래한다. 프라임 편집은 이중가닥 DNA 절단 없이 정밀한 염기 치환 및 소규모 삽입 또는 결실을 가능하게 하는 유전체 편집 기술이다.

본 연구에서는 PE2max 시스템을 활용하여 Twitcher 마우스 모델에서 GALC 유전자의 점 돌연변이를 교정하고 효소 기능을 회복시키는 Krabbe병 치료 전략을 제시하였다. Galc 유전자에서의 정확한 A에서 G로의 교정은 Galc 발현과 효소 활성을 회복시켰으며, 이는 분자적, 조직학적, 행동학적 지표의 유의미한 향상으로 이어졌다. 생후 1일에 이중 AAV 벡터 전략을 통해 PE2max를 전달하였으며, 중추신경계 표적화를 위해 AAV-PHP.eB를, 말초신경계 전달을 위해 AAV-MaCPNS1을 각각 사용하였다. 유전체 DNA와 cDNA에 대한 시퀀싱 결과, 높은 편집 정확도와 함께 오프타겟 효과는 최소 수준이었고, 삽입 및 결실은 배경 수준에서 관찰되었다. 전두엽 피질, 뇌간, 척수 등 중추신경계 영역에서는 다른 조직에 비해 높은 편집 효율이 확인되었고, 이는 Galc mRNA 발현 및 효소 활성의 증가와도 일치하였다. 이러한 변화는 수초 단백질 발현 증가, 수초 무결성 향상, 구상세포 침윤 감소 등으로도 확인되었다. 자기공명영상에서는 백질 보존이 관찰되었고, 투과전자현미경 분석에서는 치밀한 수초 구조와 정상적인 축삭이 확인되어 거시적 및 초미세구조 수준 모두에서의 회복을 입증하였다. 비록 좌골신경에서의 유전자 교정 효율은 제한적이었지만, 전반적인 안전성은 우수하였으며, 야생형과 돌연변이 마우스 모두에서 독성은 관찰되지 않았다. 이러한 결과는 PE2max 기반 프라임 편집이 이중가닥 절단 없이 질병 유발 돌연변이를 효과적으로 교정할 수 있는 정밀하고 안전한 생체 내 유전체 편집 전략임을 보여주며, 단일 유전자에 기인한 신경퇴행성 질환의 치료 가능성을 뒷받침한다.

핵심어: 크라베병, 신경퇴행성 질환, 유전자 편집, 프라임 편집, 갈락토실세라마디아제, 수초, 탈수초